HHS Public Access

Author manuscript

Acta Biomater. Author manuscript; available in PMC 2021 March 15.

Published in final edited form as:

Acta Biomater. 2020 March 15; 105: 319–335. doi:10.1016/j.actbio.2020.01.028.

Towards revealing key factors in mechanical instability of bioabsorbable Zn-based alloys for intended vascular stenting

Ehsan Mostaed[1,*], **Malgorzata Sikora-Jasinska**[2], **Morteza Shaker Ardakani**[2], **Ali Mostaed**[3], **Ian M. Reaney**[4], **Jeremy Goldman**[5], **Jaroslaw W. Drelich**[2]

[1]Department of Materials Science and Engineering, Michigan Technological University, Houghton, MI 49931, USA.

[2]Department of Materials Science and Engineering, Michigan Technological University, Houghton, MI 49931, USA.

[3]Department of Engineering Materials, University of Sheffield, Sheffield S1 3JD, UK; Department of Materials, University of Oxford, 16 Parks Road, Oxford OX1 3PH, UK.

[4]Department of Engineering Materials, University of Sheffield, Sheffield S1 3JD, UK.

[5]Department of Biomedical Engineering, Michigan Technological University, Houghton, MI 49931, USA.

Abstract

Zn-based alloys are recognized as promising bioabsorbable materials for cardiovascular stents, due to their biocompatibility and favorable degradability as compared to Mg. However, both low strength and intrinsic mechanical instability arising from a strong strain rate sensitivity and strain softening behavior make development of Zn alloys challenging for stent applications. In this study, we developed binary Zn-4.0Ag and ternary Zn-4.0Ag-*x*Mn (where *x*=0.2–0.6wt%) alloys. An experimental methodology was designed by cold working followed by a thermal treatment on extruded alloys, through which the effects of the grain size and precipitates could be thoroughly investigated. Microstructural observations revealed a significant grain refinement during wire drawing, leading to an ultrafine-grained (UFG) structure with a size of 700 nm and 200 nm for the Zn-4.0Ag and Zn-4.0Ag-0.6Mn, respectively. Mn showed a powerful grain refining effect, as it promoted the dynamic recrystallization. Furthermore, cold working resulted in dynamic precipitation of $AgZn_3$ particles, distributing throughout the Zn matrix. Such precipitates triggered mechanical degradation through an activation of $Zn/AgZn_3$ boundary sliding, reducing the tensile strength by 74% and 57% for Zn-4.0Ag and Zn-4.0Ag-0.6Mn, respectively. The observed precipitation softening caused a strong strain rate sensitivity in cold drawn alloys. Short-time annealing significantly mitigated the mechanical instability by reducing the $AgZn_3$ fraction. The

[*]Corresponding author: Ehsan Mostaed, emostaed@mtu.edu.

Declaration of interests

The authors declare that they have no known competing financial interests or personal relationships that could have appeared to influence the work reported in this paper.

ternary alloy wire showed superior microstructural stability relative to its Mn-free counterpart due to the pinning effect of Mn-rich particles on the grain boundaries. Eventually, a shift of the corrosion regime from localized to more uniform was observed after the heat treatment, mainly due to the dissolution of $AgZn_3$ precipitates.

Graphical Abstract

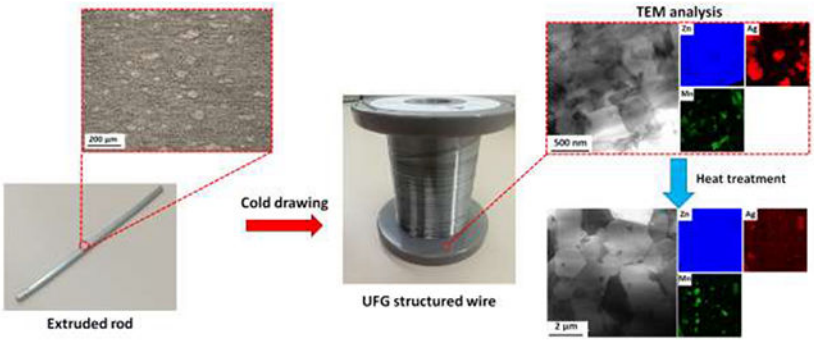

Keywords

Zinc alloys; Biodegradable; Precipitation softening; Room temperature superplasticity; Corrosion

1. Introduction

During the last two decades, bioabsorbable polymeric and metallic materials have been predominantly studied for implants in an effort to replace the permanent materials used for stents [1, 2]. Bioabsorbable stents could drastically reduce complications associated with permanent stents including chronic inflammation [3], in-stent restenosis [4], late stage thrombosis and stent strut fracture [5]. Polymeric stents, despite their predictable degradation products and acceptable biocompatibility, require a greater strut thickness than most metallic stents due to their low radial strength. Accordingly, bioabsorbable metallic materials seem to be promising candidates for stent application over their polymeric counterparts owing to their superior mechanical properties [1].

Magnesium (Mg) and iron (Fe) and their related alloys have been extensively explored as promising materials for cardiovascular stenting applications [1, 6]. Despite its excellent biocompatibility and low thrombogenicity, Mg-based materials demonstrate intrinsically rapid corrosion in physiological environments, which leads to an early undermining of the stent's mechanical integrity [7, 8]. On the other hand, while Fe-based materials exhibit superior mechanical properties, their very slow degradation rate does not allow Fe-based stents to be fully absorbed over the required service time (one to two years), leaving a large portion of the stent pristine in an implantation site [9, 10].

Since 2013, research has shifted towards bioabsorbable zinc (Zn) due to its promising biodegradability and biocompatibility [11]. Indeed, Zn's standard corrosion potential (−0.76 V) lies between Fe (−0.44 V) and Mg (−2.37 V), resulting in a favorable corrosion rate for a stent material [12]. However, Zn's poor mechanical strength has propelled researchers to

search for Zn alloys with improved mechanical properties via alloying followed by thermomechanical processing [2, 13–15]. Over the last 5 years, several alloy systems have been explored using various alloying elements including Mg [14, 16–19], Cu [20–23], Li [24–28], Ag [15, 29], Al [14, 30], Mn [28], Fe [31], Zr [32], Ca [18] and Sr [18, 33]. It has been reported that an ideal bioabsorbable stent material should exhibit tensile strength and fracture elongation exceeding 300 MPa and 25%, respectively [2, 34]. Since 2013, many research groups from around the world have been attempting to formulate new Zn alloys that meet tensile properties benchmark values, but only very few studies have claimed this accomplishment so far [26, 35]. Increasing the tensile strength of Zn alloys is at the expense of their elongation and a major challenge is therefore to preserve elongation at a value exceeding 25–30% when the tensile strength is lifted above 300–400 MPa through alloying and thermomechanical processing conditions [13]. Additional requirements that are rarely mentioned in publications on Zn-based vascular stents relate to the grain size of formulated alloys and their uniformity of corrosion. The corrosion uniformity of Zn alloys is of great importance as it prevents premature failure of the stent and reduces the variability of neointimal responses [36]. The enhanced kinetics of passivation accompanied with formation of compact protective films on the fine-grained surface of a Zn stent could suppress localized corrosion and therefore improve both its mechanical integrity and biocompatibility during the service period. Finally, control over the pronounced strain softening and strong strain rate sensitivity of formulated Zn alloys have not yet been addressed.

Zn has a very low recrystallization temperature (around 10°C) [37] and therefore undergoes dynamic recovery during deformation. This results in localization of the deformation and eventually non-uniform failure under loading. In other words, Zn alloys become softer with progressed plastic deformation. For a stent material, which is subjected to cyclic loading, the deformation localization is extremely detrimental and triggers a premature fracture of the scaffolding device. As such, suppression of the strain softening is an essential consideration for stent materials. Moreover, Zn is highly strain rate sensitive even at room temperature [38, 39]. Therefore, a stent made of Zn, which is under cyclic loading, may collapse due to creep-fatigue interaction regardless of the stress magnitude [13]. Accordingly, considering the two aforementioned mechanical-related concerns alongside the benchmark values, developing a Zn alloy suitable for stenting application seems to be more challenging than is typically discussed in published works. Indeed, to date, no Zn alloy has been introduced that satisfies the aforementioned mechanical requirements under static and dynamic loading conditions.

It is worth mentioning that metallic stents are manufactured via laser cutting of mini-tubes or wire braiding/knitting [40]. In both technologies, the material undergoes a significant cold metalworking. Surprisingly, leading research laboratories have not studied the effect of cold working on changes in microstructure, mechanical properties, and corrosion behavior of Zn-based biomaterials and stenting devices under development.

It has been reported that Zn alloys containing high-solubility biocompatible elements such as Ag are the most promising bioresorbable implant candidates since their mechanical properties could be improved through tuning the content and sizes of second phase particles [15]. In the present work, binary Zn-4.0Ag and ternary Zn-4.0Ag-xMn (where x=0.2–0.6

wt.%) alloys were formulated, processed and studied in detail. The mechanical properties of the alloys were rigorously investigated as a function of microstructure. Here, we demonstrate that the critical microstructural features including grain size and presence and distribution of precipitates dictate the mechanical characteristics of Zn-based alloys. We systematically evaluated the individual and combined effects of these factors on the mechanical properties and stability of the alloys. In addition, it is demonstrated that the microstructure design in Zn alloys can be used to find an optimum and effective strategy to not only improve the mechanical properties but also to minimize any damage by augmenting the corrosion uniformity and mechanical integrity of the alloys.

2. Experimental procedures

2.1. Materials and their processing

In this study, binary Zn-Ag and ternary Zn-Ag-Mn alloys were formulated and investigated. The as-cast alloys (Table 1) in the shape of cylindrical billets with a diameter of 30 mm were produced by melting stoichiometric quantities of Zn shots (99.995%), Ag shots (99.95%) and Mn powder (99.995%) at 700 °C in cylindrical graphite crucibles inside a resistance furnace. Annealing at 400 ˚C was conducted for 2h (binary alloy) and 8h (ternary alloys) in order to homogenize the cast structure, followed by water quenching. Annealed samples were subsequently extruded at 310°C with an extrusion ratio of 39:1 to obtain cylindrical rods. The extruded rods of 4 mm in diameter were centerless ground to provide a pristine surface finish and were then multi-pass drawn at room temperature into wires with a diameter of 0.25 mm by Fort Wayne Metals (Fort Wayne, IN). The strain was calculated by area reduction (AR) using the following equation:

$$AR = \frac{A0 - Af}{A0} \times 100 \quad (1)$$

where A_0 and A_f denote the initial and final cross-sectional area. According to Eq. 1, the wires were drawn with an accumulative AR of 99.6%. Selected cold drawn wires were annealed at 360°C for 2s to 60 min of soaking times.

2.2. Microstructural analysis

All the investigated samples were cut to longitudinal (i.e. parallel to the extrusion direction) sections. The samples were ground and polished following standard metallographic procedures and etched with a 3% Nital solution (3 ml. HNO_3 + 100 ml. ethanol). Microstructure was recorded by optical microscopy (OM) and PHILIPS XL 40 scanning electron microscopy (SEM) operating at 15kV. The evolution of the structure in extruded samples was assessed primarily by examination of longitudinal sections. Microstructural characterization of cold drawn (CD) and heat treated (HT) wires was carried out on their longitudinal sections. Grain size distributions, crystallographic texture and grain orientation maps were obtained using electron backscattered diffraction (EBSD) in SEM. An accelerating voltage of 20 kV, a working distance of 8 mm, step size of 0.3 μm and a sample rotation angle of 70°, were selected to maximize the indexing of Kikuchi patterns. The EBSD data was processed with AZtecHKL software. X-ray diffraction (XRD) was carried out on the cast alloys for phase identification using an XDS 2000θ/θ diffractometer (Scintag

Inc., Cupertino, CA) with CuKα radiation ((λ = 1.540562 Å). XRD patterns were collected from 2θ range of 20–90° with a scan speed of 0.5°/min and a step size of 0.02°. Transmission electron microscopy (TEM) samples were prepared using standard routes, i.e. grinding and polishing the specimens to < 40 μm followed by ion beam milling to electron transparency. Ion beam milling was performed at liquid nitrogen temperature by a GATAN precision ion polishing (PIPS) II using Ar^+ initially at 5 keV and final milling at 1 keV. Transmission electron microscopy was performed on JEOL JEM F200 and JEOL R005 operating at 200 kV and 300 kV, respectively. The grain size of the alloy wires was calculated by ASTM E112–96 standard according to the linear intercept procedure.

2.3. Mechanical characterization

Mechanical properties after extrusion and wire drawing were evaluated by tensile testing. Tensile specimens with long axis along the extrusion direction were machined from extruded billets with a gage length of 12 mm and diameter of 4 mm. Tensile testing on the extruded rods was performed at an initial strain rate of 3.3×10^{-3} s^{-1} using an MTS Insight™ 4206 machine with a maximum force capacity of 45 kN. Tensile tests on wires (both the CD and HT wires) were carried out on segments with a gauge length of 40 mm using a 1.0 kN load cell. Tensile testing on the wires was conducted at strain rates ranging from 3.3×10^{-4} s^{-1} to $2.7 \times 10^{-1} s^{-1}$.

2.4. Corrosion behavior

The corrosion behavior of Zn-Ag and Zn-Ag-Mn wires before and after the heat treatment was evaluated by in vitro immersion tests in a Hanks' solution. The tests were carried out according to the ASTM G31–72 standard. The solution was prepared with 9.5 g of balanced Hanks' salts (H1387, Sigma-Aldrich) in 1 L of distilled water supplemented with 0.35 g of $NaHCO_3$ (S8875–500G, Sigma Aldrich). The solution pH was adjusted to 7.4 by the addition of 1M HCl or 1M NaOH, where appropriate. The weight, length and cross-sectional diameter of the samples were measured prior to immersion. For each condition, four wires with a length of 30 mm were immersed for 10 and 40 days in Hanks' solution. The containers were stored in a controlled environment (T = 37±1°C), with a CO_2 atmosphere content of 5 vol. % and a relative humidity of 85%. The solution volume for each sample was specified by the aforementioned standard, for a total of ~ 50 mL per sample. Subsequently, the wires were washed with 70% ethanol in an ultrasonic bath for 5 minutes, in order to remove the non-adherent corrosion precipitates formed on the surface before measuring the final weight. The cross-sectional diameter of the immersed wires was calculated as an average of several readings to ensure an accurate measurement. Corrosion rates were calculated using the weight loss method, following the equation:

$$CR = \frac{W \cdot d}{4 \cdot m \cdot t} \quad (2)$$

CR is the corrosion rate ($mm \cdot year^{-1}$), W is the weight loss (g), m is the wire mass (g), d is the wire diameter (mm), and t is the exposure time (years).

2.5. Statistical analysis

In this study, the experimental results are presented as the mean ± standard deviation unless otherwise noted. For each group of alloys, the standard deviation was calculated out of three experiments.

3. Results and discussion

3.1. Alloys processing and characterizations

3.1.1. Microstructure of the as-cast and solution treated alloys—Representative optical micrographs of the as-cast and solution treated alloys are displayed in Fig. 1. The microstructure of the as-cast alloys (Fig. 1a–d) consist of primary η-Zn phase along with secondary phase dendrites. Moreover, the larger Mn content leads to an increase in the volume fraction of the secondary phases (Fig. 1b to d). The microstructural evolution of the alloys after the solution heat treatment is presented in Fig. 1a'–d'. In the alloys with up to 0.4 wt.% of Mn addition (AM44), solution treatment results in forming a supersaturated solution of Ag and Mn in η-Zn. However, in the alloys containing Mn > 0.4 wt.%, the secondary phases with a block-shaped morphology are present and distributed throughout the Zn matrix even after the solution treatment. Furthermore, the addition of Mn significantly reduces the grain size of the solution treated alloys (from > 1 mm for A4 to about 80 μm for AM46) through the solute dragging effect on grain boundaries, which restricts grain growth by decreasing grain boundary mobility [41].

XRD patterns of the cast alloys are shown in Fig. 2. The analysis for the A4 alloy reveals that only two phases of η-Zn solid solution and primary ε-$AgZn_3$ were formed. Hence, the dendritic secondary phase shown in Fig. 1a is $AgZn_3$. These results are consistent with the observations by Sikora-Jasinska et al. [15] who reported that the $AgZn_3$ phase forms in the Zn-Ag binary alloys with an Ag content higher than 2.5 wt.%. For all the ternary alloys, regardless of the Mn concentration, the patterns merely present peaks corresponding to the η-Zn solid solution and ε-$AgZn_3$. It should be highlighted that as the Mn content is very low in the ternary alloys (below 0.6 wt.%), the XRD patterns could not reveal information about the role of Mn in the microstructure of these alloys. However, using electron microscopy, we will show later that Mn-rich particles decorate the grain boundaries.

3.1.2. Microstructure of the extruded alloys—Fig. 3 shows the microstructure of the alloys after hot extrusion. Combined analysis of Fig. 1a and Fig. 3a indicates that the extruded A4 alloy has significantly smaller equiaxial grains (~18 μm) than its solution treated counterpart (> 1mm). This suggests that hot extrusion is an effective grain refinement method for Zn alloys. Figs. 3b–d show that Mn addition results in the formation of a bimodal grain structure in the extruded alloys, where coarse and non-recrystallized grains (> 200 μm) are surrounded by a large number of dynamically recrystallized (DRXed) grains with a size of a few micrometers. The DRXed grains are located in places where most of the secondary-phase particles exist, which is attributed to the phenomenon of particle stimulated nucleation (PSN) [42]. This initiates formation of high-stress zones around hard secondary phases, accelerating the DRX process and promoting grain refinement. It is evident that with increasing Mn content from 0.2 wt.% to 0.6 wt.%, the fraction of the non-recrystallized

grains drastically decreases as a result of the presence/absence of the $AgZn_3$ phase and Mn-rich particles in the solution treated samples. As already presented in Figs. 1b' and 1c', AM42 and AM44 alloys exhibit a single-phase microstructure in their solution treated condition. In alloys containing 0.6 wt% Mn, secondary phases are present at the grain boundaries, which act as preferential sites for dynamic recrystallization nucleation (Fig. 1d'). Therefore, as shown in Fig. 3d, any Mn addition higher than 0.4 wt.% in the ternary alloys leads to an increase in the fraction of the DRXed grains at the expense of large deformed grains, causing further grain refinement.

3.1.3. Texture evolution of the extruded alloys—Fig. 4 presents the EBSD maps and corresponding inverse pole figures (IPFs) recorded for the ED-ND planes of the A4, AM44 and AM46 extruded alloys. It is hypothesized that an increase in the local stress concentration promoted by larger fractions of Mn-rich particles stimulates the DRX and thus promotes a more effective grain refinement. Hence, the mean grain size of the A4 alloy decreases in ternary alloys with increasing Mn content, from 18 μm in A4 to 2.4 μm in AM44 and 1.8 μm in AM46. The IPF analysis indicates a strong basal texture of the A4 alloy, where the majority of basal planes are parallel to the extrusion direction. However, with Mn addition and increasing content, the maximum texture intensity gradually decreases from 6.52 for A4 to 3.76 for AM44 and 2.69 for AM46. Moreover, Mn addition develops a random distribution of basal planes towards the extrusion direction ED; basal planes are tilted toward $[10\bar{1}0]$ and $[2\bar{1}\bar{1}0]$ poles. Such random distribution is more pronounced for the AM46 alloy. Indeed, there are more randomly oriented grains in AM46 than AM44 (compare IPFs in Figs. 4b and c). This implies that the addition of Mn induces basal texture weakening in the Zn-Ag alloy system, which is similar to the well-established effect of Ca addition to Mg alloys, and could therefore develop texture randomization through the PSN of recrystallization [43]. The weak basal texture, especially in AM46 alloy, is more favorable for basal dislocation slip during tensile testing when the applied load is along the extrusion direction, which overall might significantly improve the alloy's ductility.

3.1.4. Mechanical properties of the extruded alloys—Fig. 5 summarizes the tensile characteristics of the investigated alloys with respect to the benchmark values of tensile strength (> 300 MPa) and elongation to failure (> 25%) required for an ideal absorbable stent material. A small addition of Mn (0.2 wt.%) to Zn-4Ag leads to a noticeable increase in tensile strength from 228 ± 5 MPa to 267 ± 9 MPa. Further addition of Mn consistently enhances the tensile strength to 281 ± 5 MPa and 302 ± 7 MPa for AM44 and AM46 alloys, respectively. Indeed, the improvement in tensile strength is attributed to the formation of the Mn-rich particles, located at the grain boundaries. An increase in Mn concentration promotes the grain refining effect through PSN phenomenon (Fig. 3 and Fig. 4). Interestingly, the fracture elongation of the investigated ternary alloys not only remains above the benchmark value but also rises with increasing Mn content. AM46 shows the highest elongation (35 ± 4%) among the investigated alloys (27 ± 3%, 25 ± 6% and 29 ± 3% for A4, AM42 and AM44, respectively). It is known that thermo-mechanically processed Zn alloys with poor ductility consist of sharp-edged and coarse brittle intermetallic phases that are nonuniformly distributed within the Zn matrix [13]. The absence of any coarse and brittle phases implies the reasonably high elongation of the alloys. More importantly, as

shown in Fig. 4, the texture randomization generated by Mn addition results in an easy dislocation slip on the dominant slip plane (0002) and thereby improves the alloy's ductility at room temperature. In brief, the combined effects of grain refinement hardening, second phase strengthening (markedly fine and uniformly dispersed Mn-rich particles throughout the Zn matrix) and favorable texture orientation produce a meaningful improvement in tensile strength in the AM46 alloy, while maintaining a remarkably high fracture elongation. Accordingly, Fig. 5 reveals that the AM46 alloy successfully fulfills the mechanical requirements for a stent material. It should be noted that in Fig. 5, except for Zn-0.8Li-0.2Mg and Zn-0.8Li, no other alloys have yet been reported in the literature that could meet the tensile benchmark values. However, the stress-strain curves of the Zn-0.8Li-0.2Mg and Zn-0.8Li alloys indicate that they undergo a remarkably strong strain softening, reaching an early peak flow after only 5% of deformation followed by decreasing stress with the progression of strain [26, 35]. These alloys are not ideal for stent materials as they are prone to the localization of deformation and may therefore experience premature fracture during service.

3.2. Wire drawing

3.2.1. Microstructural and mechanical characterizations of the wires—Metallic stents are manufactured via either tube laser cutting or wire braiding. In both technologies, the metals used to manufacture mini-tubes and wires experience massive cold working, which affects the microstructure and consequently the mechanical characteristics of the stent. To explore the effect of cold working, AM46 alloy with the best combination of strength and ductility (Fig. 5) was selected for wire drawing. For comparison purposes, the binary A4 alloy was also cold drawn. Fig. 6 shows bright-field STEM images as well as EDS elemental maps recorded for the cold drawn (CD) A4 and AM46 alloys. As shown in Fig. 6a, the microstructure of A4 was significantly refined down to an ultrafine-grained (UFG) structure (grain size of about 700 nm) after drawing. Surprisingly, as shown in Fig. 6a, the EDS elemental maps of the CD A4 wire reveal submicron Ag-rich precipitates (within a size range of 100 – 500 nm), uniformly dispersed throughout the Zn matrix. On the contrary, the A4 alloy prior to wire drawing featured a single-phase structure in the extruded condition (Fig. 3a). Indeed, when a non-equilibrium solid solution alloy (like the A4 alloy here) is refined down to UFG regime and simultaneously subjected to severe plastic deformation, it experiences a dynamic precipitation of secondary phases. Moreover, the density of grain boundaries, considered as high speed diffusion pathways, dramatically increases in alloys when they are refined down to UFG microstructure [44]. An increased density of grain boundaries magnifies the diffusion of Ag solute atoms from the Zn matrix during cold working even at a room temperature, accelerating the formation of Ag-rich precipitates. Interestingly, as illustrated in the EDS elemental maps presented in Fig. 6a, the majority of Ag dissolved in the Zn matrix was consumed for formation of the Ag-rich precipitates and a very small quantity of Ag remains in the Zn solid solution. It is therefore concluded that Zn-based alloys are strongly vulnerable to dynamic precipitation when they are subjected to a massive cold working. Accordingly, alongside significant grain refinement (known as Hall-Petch strengthening), the deformation-induced precipitates should have a crucial role in the mechanical properties of the drawn wires. This might change the current paradigm of the mechanical benchmarks for the thermo-mechanically processed Zn-based

alloys reported in the previous section. Since 2014, all publications in the domain of Zn-based alloys for vascular stenting applications have relied on the aforementioned benchmarks for the hot rolled/extruded alloys. Several of these have reported alloys exhibiting mechanical properties close to or exceeding the tensile benchmark values as possible stent material candidates. Contrarily, this study reveals that the selection of materials for bioresorbable stents cannot be limited to mechanical testing on raw Zn-based materials prior to stent manufacturing steps that involve cold drawing.

The phenomenon of room temperature dynamic precipitation was recently discovered by our group in the Zn-Cu alloy system [38]. In the case of the AM46 wire, as shown in Fig. 6b, the microstructure after wire drawing is markedly more refined than that of the A4 wire (200 nm vs 700 nm). This refinement is attributed to the extremely fine Mn-rich particles dispersed in the matrix (see EDS maps in Fig. 6b), which firstly amplify the dynamic recrystallization and eventually hinder the growth of the newly recrystallized UFG grains during the drawing process. In addition, we observed reflections for pure Mn in the selected area diffraction (SAD) patterns obtained from the CD AM46 alloy (e.g. Fig. 6c), implying that those Mn-rich particles highlighted in Fig. 6b are most likely pure Mn particles. Figure 7 shows bright-field, dark-field and HRTEM images obtained from one of those Mn-rich particles. As the dark-field image displayed in Fig. 7b is formed by contribution of diffracted electrons from Mn {233} ($1/d \approx 5.3\ 1/nm$) and Mn {224} (i.e. $1/d \approx 5.5\ 1/nm$), the particle with the bright contrast in this image is a Mn nanoparticle. Further examination of this nanoparticle by HRTEM (Figs. 7c and 7d) confirms that such Mn-rich nanoparticles are pure Mn. Although the presence of $MnZn_{13}$ was reported in Zn-Mn-Fe [45] and Zn-Mn-Ca [46] alloy systems, the Zn matrix in AM46 alloy is not thermodynamically similar to those in Zn-Fe or Zn-Ca alloys since Ag, unlike Fe and Ca with no solubility in Zn, can dissolve in Zn (up to 8 wt.%) [13]. Accordingly, the formation of pure Mn in AM46 alloy might be due to an increment in the formation energy of $MnZn_{13}$ phase as a result of dissolved Ag in the Zn matrix. Furthermore, similar to the A4 alloy, the EDS elemental maps recorded for the AM46 alloy show the presence of nanosized $AgZn_3$ particles, indicating the occurrence of dynamic precipitation of nanosized $AgZn_3$ particles at the expense of Ag solute in the Zn matrix.

The above-mentioned results indicate that the cold working process causes grain refinement as well as formation of the deformation-induced precipitates in Zn-based alloys. Therefore, according to the classical metal working principles, we expect the CD wires to exhibit significantly high strength due to the promotion of grain boundary and precipitation hardening mechanisms. Remarkably, as shown in Fig. 7, both the A4 and AM46 alloys lost their strength and became exceptionally soft after cold working. These reductions in the tensile strength are about 74% and 57% for the A4 and AM46 alloys, respectively. This means that not only the mentioned hardening mechanisms have no contributions to the strengthening of the alloys but also additional softening mechanisms were introduced. As shown in Fig. 7a, the CD A4 alloy exhibits a reduced peak flow followed by a pronounced strain softening, leading to a remarkably large elongation to failure of 430% at the strain rate of $3.3\times10^{-3}s^{-1}$. In the case of CD AM46, however, besides a lower reduction in tensile strength, the fracture elongation is less than half that of A4 (203% vs 430%). Based on tensile testing results (Fig. 7), it is concluded that although both CD alloys represent softening and improved ductility compared to their EX counterparts, the softening

contribution for the CD AM46 is significantly lower than that for CD A4. This difference is attributed to the presence of nanosized Mn particles, which is discussed later.

In order to examine the effects of strain-induced precipitates and grain refinement on the tensile properties of the alloys, CD alloys were heat treated at 360°C for various times (from 2s to 60 min) and their tensile properties were evaluated at the strain rate of 3.3×10^{-3} s^{-1}. Fig. 8a presents the tensile curves of the CD A4 alloy at different heat treatment (HT) times. Surprisingly, the peak flow drastically raises by 173% from 60 MPa to 164 MPa accompanied by a nearly 72% drop in elongation after only 2s. Microstructural analysis reveals a slight grain growth from ~700 nm (Fig. 6a) to ~1 μm (Fig. 9a) after 2s of HT. This small grain growth cannot account for such a drastic change in the mechanical properties of this alloy. Instead, we also noticed a large decrease in the $AgZn_3$ volume fraction after 2s of HT from 29% to 8%. Therefore, strain-induced precipitates are believed to be responsible for the drastic changes in mechanical properties. The abnormal softening behavior induced by cold working in Zn-based alloys was named “precipitation softening” in our earlier contribution by Mostaed et al. [38]. As the diffusion at $Zn/AgZn_3$ interphases is significantly higher than at Zn/Zn, the remarkably fine $AgZn_3$ precipitates offer additional interfaces to take part in phase boundary sliding, which is the rate-controlling mechanism during the deformation.

Despite the large increase in tensile strength, the 2s-HT A4 alloy (similar to its CD counterpart) still suffers a pronounced work softening, demonstrating a premature UTS followed by a drop in stress for larger strain values. Figs 9a and 9b show that continuation of the HT from 2s to 10s leads to further grain coarsening from ~1.0 μm to ~2.1 μm, an increase in the peak flow from 164 MPa to 186 MPa, and a slight mitigation of the strain softening (Fig. 8a); the peak flow occurs at 8% and 42% of strains after 2s and 10s of HT, respectively.

Furthermore, Figs 9a and 9b reveal that 10s of HT not only causes grain growth, but also remarkably decreases the volume fraction of $AgZn_3$ precipitates, highlighting the paramount effect of precipitates on the mechanical instability of the A4 alloy. Eventually, after 20s of HT, $AgZn_3$ precipitates are not visible in micrographs and probably dissolve completely in the Zn matrix (Fig. 9c). The formation of a single-phase structure is accompanied by a maximum strength (189 MPa) and, more importantly, suppression of the strain softening. Figs. 9d and 9e indicate that any HT time greater than 20s results in a significant grain growth due to the absence of $AgZn_3$ precipitates, which pin the grain boundaries. The CD A4 wires show grain sizes of ~16 μm and ~37 μm after 1 min and 2 min of HT, respectively. Such coarse grain structures lead to a reduction of the yield strength along with a very strong strain hardening rate, associated with the activation of twins during tensile deformation [38, 47].

Fig. 8b presents the average values of 0.2% offset proof stress as a function of grain size for the A4 alloy. It is seen that grain refinement down to 2.3 μm improves the yield strength of the A4 alloy and below which any further refinement softens the material. In fact, the A4 alloy exhibits an inverse Hall-Petch relationship when its grain size is below 2.3 μm. It is well documented that the Hall-Petch effect is reversed for nanocrystalline metallic materials

(grain size on the order of 10 nm-30 nm) [48]. However, we found that such inverse Hall-Petch occurs for the A4 alloy at a significantly larger grain size. Therefore, it can be concluded that the A4 alloy exhibits a decreased yield strength with a grain size below ~2.3 μm. However, the deformation localization, which arises from strain softening, can be suppressed only if the grain size is above ~3.5 μm (i.e. after 20s of HT). Accordingly, the best mechanical properties for the A4 alloy are obtained when the grain size exceeds 3.5 μm.

To date, several research works have suggested the mechanical properties enhancement of Zn alloys through grain refinement down to the ultrafine regime (below ~1 μm) [49, 50]. This statement is correct for other metallic bioresorbable metals such as Mg [8, 51] and Fe-based [52] alloys. The present study demonstrates that any processing strategies that result in a refined microstructure, such as severe plastic deformation, should be avoided for Zn-based alloys as they promote precipitation softening-induced mechanical degradation.

Fig. 10a shows RT tensile properties of the CD A4 alloy at various strain rates. It is evident that this alloy in CD condition is strongly strain rate sensitive so that with increasing the strain rate from 3.3×10^{-4} s^{-1} to 2.7×10^{-1} s^{-1} the peak flow markedly increases from 57 MPa to 259 MPa (> 350%), respectively. Such a strong strain rate sensitivity is of major concern for a stent material, which undergoes cyclic loading and may collapse in the blood vessel due to creep-fatigue interaction. Moreover, the CD A4 alloy exhibits a distinct strain softening behavior over all the tested strain rates. This is an additional mechanical-related concern that points to deformation localization and a possibility of premature failure of the stent during service. However, as shown in Fig. 10b, the 20 s-HT A4 alloy shows a significantly lower susceptibility to the strain rate. Indeed, the peak flow increases from 130 MPa to 227 MPa (i.e.75% increase) as the strain rate rises from 3.3× 10−4 s−1 to 2.7× 10−1 s−1, respectively.

Fig. 10b shows that the tensile curve for the HT A4 alloy tested at the strain rate of 2.7× 10−1 s−1 experiences a serrated flow. This is ascribed to the activation of deformation twining. In HCP materials, such as Mg and Zn, deformation twinning plays a crucial role in the accommodation of plastic strain during the deformation. At high strain rates the contribution of twining to the deformation is more pronounced, featuring a serrated flow in the tensile curves. In contrast, the CD A4 alloy tested at a high strain rate (2.7× 10−1 s−1) does not feature the serration phenomenon (Fig. 10a). It is proved that decreasing the grain size increases the critical resolved shear stress for the twining and thereby suppresses the activation of twining [53]. Similarly, for the CD alloys with UFG structures no serrated flow was observed even at high strain rates, confirming the operation of dislocation slip as a dominant deformation mechanism.

Fig. 10c shows the variation of flow stress against the initial strain rate, where the flow stress for each strain rate is determined at a strain of $\varepsilon = 0.1$. As shown, the flow stress for both the CD and 20 s-HT A4 alloys invariably increases with increasing the strain rate although this trend is more pronounced for the CD alloy. It is well known that for the superplastic alloys the strain rate sensitivity exponent (m), defined as the slope in a double logarithmic plot of flow stress versus strain rate, should be above 0.4 [54].

The sigmoidal shape of the curve for the CD A4 alloy is indicative of its superplastic behavior. Both the maximum m value and elongation are achieved in the intermediate stress region (region II). Such a high value of m (0.41) supports the hypothesis that slip-accommodated grain boundary sliding (GBS) dominates the deformation, leading to a maximum elongation of 430% at 3.3×10^{-3} s^{-1}. However, the m value and fracture elongation significantly decrease at higher strain rates (region III), suggesting that the rate-controlling deformation process is dislocation slip [54]. It is well documented that grain refinement in metals enhances the superplastic ductility [55, 56]. Superplasticity is a diffusion-controlled process requiring temperatures above $0.5T_m$ and grain size smaller than 10 μm [57]. It is well-documented that superplasticity could occur even at temperatures below $0.5T_m$ in metals with fine microstructures [57]. Thus, the observed room temperature superplasticity (RTS) in the CD A4 alloy is attributed to the UFG structure. Metals with superplastic behavior exhibit decreased m values at low strain rates (region I) due to the microstructural instability arising from grain coarsening. However, the lack of grain growth occurrence at RT for the CD A4 alloy suggests that the low m value in the low-strain rate range is attributed to the existence of a threshold stress, which results from the interaction of solute atoms with the grain-boundary dislocations [58]. It has been reported that the required stress to break away the grain-boundary dislocations from their solute atmospheres formed at the grain boundaries represent the threshold stress [58]. Interestingly, the measured m values for the HT A4 alloy, which features a single phase structure and an average grain size of 3.5 μm (Fig. 9c), are significantly smaller than those for the CD alloy over all the tested strain rates. Hence, the HT A4 alloy shows less susceptibility to the strain rate. In particular, the maximum m value in the intermediate stress region drops from 0.41 to 0.08 after HT, implying the transition of deformation mechanism from the GBS to dislocation slip. This causes a marked drop in the fracture elongations for the HT A4 alloy, especially at low strain rates (e.g. from 430% to 80% at the strain rate of 3.3×10^{-3} s^{-1}).

It is worth mentioning that although 20s of HT causes a notable grain growth (from 0.7 μm to 3.5 μm), the microstructure of the HT sample is still fine enough to experience RTS. However, Figs. 10b and c clearly indicate that RTS is not operative for the HT A4 alloy. This suggests that the GBS is not the dominant flow mechanism in the HT A4 alloy and therefore the RTS is strictly governed by deformation induced $AgZn_3$ precipitates.

Although the GBS mechanism was ascribed to the improved fracture elongation in UFG Zn alloys in some recent studies [59, 60], our findings reveals that the underlying mechanism for this improvement arises from the dynamic precipitation of $AgZn_3$ nanoparticles. This phenomenon occurs only in UFG Zn alloys consisting of markedly refined precipitates, where the density of Zn/precipitate interphase boundaries is considerably high. Precipitation hardening is a well-documented process in all ferrous and nonferrous alloys with the ability of second phase precipitation. However, in this work we present a new terminology of “precipitation softening” which is active in a wide range of UFG Zn alloys (e.g. Zn-Cu, Zn-Mn, Zn-Ag, Zn-Al etc.). It should be highlighted that such a microstructure cannot be obtained by conventional thermomechanical treatments. In fact, the UFG structure in Zn alloys can be achieved only by applying repetitive cold working or severe plastic deformation techniques, through which massive plastic deformation can be imposed on the alloy [38, 56].

Previous studies on double phase eutectoid Zn-22Al alloy with an UFG structure showed that less sliding occurs at Zn/Zn boundaries in comparison to Zn/Al interface boundaries [57]. Accordingly, we assume that the activation energy for sliding at Zn/$AgZn_3$ interphases is much lower than that at Zn/Zn. Thus, the remarkably fine $AgZn_3$ precipitates provide an abundant number of interfaces to take part in phase boundary sliding (PBS). The presence of these precipitates facilitates the sliding mechanism and RTS is therefore mainly dictated by PBS rather than GBS. This highlights the dominant effect of precipitates over grain size on the mechanical properties of Zn alloys so that with a slight modulation in their fraction a wide range of properties could be acquired.

Fig. 11a shows the tensile curves of the CD AM46 alloy after HT at 360°C for 1 to 60 min. After a short-duration HT (1 min) almost the entire mechanical strength is restored at the expense of ductility. Indeed, 1 min of HT leads to an increase in the UTS from 124 MPa to 301 MPa accompanied by a sharp drop in the fracture elongation from 204% to 19%. The origin of this behavior lies in the change of microstructure after HT. For example, our STEM results show that while there is a subtle grain growth from 200 nm (Fig. 6b) to 300 nm (Fig. 12a) for the CD and 1 min-HT AM46 alloys, respectively, the size of deformation-induced $AgZn_3$ precipitates doubled or tripled after 1 min of HT. In addition, the EDS results, presented in Fig. 12a, indicate the dissolution of Ag in Zn matrix grains after 1 min of HT, which promotes the solid solution strengthening mechanism and therefore improves the tensile strength. Surprisingly, nanosized Mn-rich particles are uniformly distributed at grain boundaries, which have a hindering effect on the movement of grain boundaries and remarkably retard the grain growth process. Thus, the notable improvement of the tensile strength for the 1 min-HT AM46 alloy is related to a combination of the above-mentioned factors namely; (i) reduction of the $AgZn_3$ nanoprecipitates fraction (suppression of precipitation softening), (ii) promotion of solid solution strengthening due to the dissolution of Ag in the Zn matrix and (iii) presence of nanosized Mn-rich particles pinning the grain boundaries, which promote particle dispersion strengthening. The latter case is counterbalanced by precipitation softening and the lack of solid solution strengthening for the CD AM46 alloy, which results in a very low tensile strength (Fig. 11a).

As presented in Fig. 11a, the 1 min-HT AM46 alloy exhibits an evident strain softening behavior during tensile testing, despite a high tensile strength. Continuation of HT to 12 min leads to a consistent decrease in tensile strength from 301 MPa to 252 MPa and an improvement in elongation from 19% to 47%. More importantly, with increasing HT duration the strain softening behavior is gradually reduced. Eventually after 12 min of HT it is fully suppressed in a way that the stress-strain curve is almost flat, suggesting that there is a dynamic balance between hardening and softening. Fig. 11a shows that further HT up to 20 min could slightly enhance the tensile strength to 257 MPa and generate strain hardening without sacrificing the fracture elongation. Fig. 12b demonstrates a considerably refined grain structure of the HT AM46 alloy wire after a relatively long HT time of 20 min, implying the outstanding microstructural stability of this alloy. The EDS elemental map analysis on the 20 min-HT AM46 (Fig. 12b) shows the significant enrichment of Zn matrix with Ag which is due to dissolution of the deformation-induced $AgZn_3$ precipitates into the matrix. In addition, the presence of thermally stable Mn-rich particles still features their distinguished pinning effect on the grain boundaries, which restrains the grain coarsening

and retains the grain significantly small (around 1.2 μm). Compared to the binary A4 alloy wire, which experiences an abnormal grain growth even after 1 min of HT (from 0.7 μm to 18 μm), the Mn-containing alloy (AM46) exhibits an extraordinary thermal stability even for longer HT times. It should be emphasized that HT was conducted at a very high temperature (360°C) in this study, which corresponds to nearly 91% of the alloy's melting point. To date, such an exceptional microstructural stability has not been reported for Zn-based alloys in the literature.

From Fig. 11a it can be seen that increasing the HT time from 20 min to 60 min lowers the tensile strength and improves the strain hardening rate, which is attributed to the additional grain growth.

The Hall-Petch relationship for the AM46 alloy is plotted in Fig 11b. Similar to the CD A4 alloy, CD AM46 features an inverse Hall-Petch effect. However, the critical grain size for AM46 is much lower than that of A4 (0.42 μm vs 2.3 μm). The AM46 alloy retains its strain softening behavior as long as its grain size is below 1.2 μm, while this strain softening suppression for the A4 alloy was observed at the grain size of 3.5 μm. Indeed, the AM46 alloy features softening susceptibility at lower grain sizes than that found in the A4 alloy. It is therefore concluded that applying grain refinement to the A4 and AM46 alloys down to the submicron regime is of critical concern, resulting in mechanical instability arising from the dynamic precipitation of $AgZn_3$ particles.

The 20 min-HT AM46 alloy was selected for the strain rate susceptibility studies because it exhibited the best combination of strength, ductility and lack of strain softening. The CD AM46 alloy wire was also tested for comparison purposes. The tensile behavior of the CD and 20 min-HT AM46 alloy wires tested at a wide range of strain rates are presented in Figs. 13a and 13b. CD AM46 is susceptible to the applied strain rate although the sensitivity is not as strong as that measured for the CD A4 alloy. As mentioned previously, despite a significantly finer microstructure for CD AM46 relative to CD A4 (see Fig. 6), less strain rate sensitivity and a lower fracture elongation was measured over all the strain rates (Fig. 13a vs Fig. 10a). This is attributed to the presence of nanosized Mn-rich particles which are distributed at the grain boundaries, impeding the grain boundary mobilities and thereby reducing the contribution of PBS to the deformation of the CD AM46 alloy. Interestingly, Fig. 13b demonstrates that 20 min of HT results in a remarkably reduced sensitivity to strain rate in a manner that constrains the maximum flow stress range between 247 MPa and 285 MPa for strain rates ranging from $3.3\times 10^{-4}\ s^{-1}$ to $2.7\times 10^{-1}\ s^{-1}$. Further, the strain softening behavior for the 20 min-HT AM46 is successfully suppressed over the investigated deformation rates and is replaced by strain hardening at strain rates exceeding $3.3\times 10^{-4}\ s^{-1}$. Accordingly, it can be concluded that the strain rate sensitivity strongly depends on the fraction of strain-induced precipitates while, interestingly, the strain softening is mainly dictated by grain size, appearing in the AM46 alloy with a submicron structure.

A comparison of Fig. 13c and Fig. 10c reveals that the m value for the CD AM46 alloy in the intermediate stress region is lower than that measured for the CD A4 alloy (0.21 vs 0.41), suggesting a lower contribution of PBS to the deformation due to the pinning effects of nanosized Mn-rich particles. This leads to a decrease in fracture elongation (204%) for

the CD AM46 alloy despite its remarkably finer grain structure than its Mn-free counterpart (200 nm vs 700 nm). Therefore, trace addition of Mn could result in a transition of the dominant deformation mechanism from PBS to dislocation slip and thereby suppress RTS. Similar to the binary alloy, HT reduces the m values at all tested strain rates in the AM46 alloy. However, as depicted in Fig. 13c in the case of the Mn-containing alloy, this reduction is remarkably high so that the measured m values are close to zero (0.03, 0.02 and 0.02 in the region I, II and II, respectively). Such a drastic reduction in the m values, which makes the plot of flow stress against strain rate nearly flat, confirms the successfully subdued strain rate sensitivity in the 20-min HT AM46 alloy.

The mechanical instability observed in the CD wires breaks the current paradigm of mechanical properties requirement. We found that the tensile properties of the thermomechanically processed Zn alloys do not reflect the properties of the laser cut or wire braided stents. Applying cold processing on the hot extruded/rolled Zn alloys may remarkably alter their mechanical behavior. This implies that researchers working on this class of materials should also consider the evaluation of material in its possible final products.

3.2.2. Corrosion behavior of the wires—In order to examine the influence of the microstructural features on the initiation and development of corrosion on the surface of Zn alloy wires, an immersion test was carried out on the A4 and AM46 alloy wires in both the CD and HT conditions. Representative backscatter images of cross sections of the A4 and AM46 wires after 10 and 40 days of immersion are shown in Fig. 14. Pairwise comparison of the CD and HT conditions for both the A4 and AM46 alloys clearly demonstrates that the corrosion behavior of Zn alloys is strongly dictated by the alloy processing history. It is well-documented in all metallic materials that cold working impairs corrosion resistance as it introduces strain-induced crystalline defects, such as high-energy grain boundaries (subgrain boundaries), dislocations and twins [61]. In the case of our Zn alloys, however, due to their low recrystallization temperature, the stored energy derived from CD is consumed on the formation of strain free DRX grains (see Figs. 6a and b). Accordingly, the reduced corrosion resistance of the CD A4 and AM46 alloys is not related to the introduced microstructural defects. In addition, as shown in the previous section, a slight grain coarsening occurred after HT (from 0.67 μm to 3.5 μm for A4 alloy and from 0.24 μm to 1.2 μm for AM46 alloy). However, this minor grain growth is not responsible for such a drastic change in the corrosion response of the alloys, demonstrated by micrographs and corrosion rate values in Fig. 14. As such, considering the microstructural difference between the CD and HT wires, the accelerated corrosion rate of the CD wires is attributed to the presence of the deformation-induced $AgZn_3$ precipitates, which enhance micro-galvanic coupling. Nevertheless, previous research works [15, 21–23] reported that Zn, unlike Mg, is not highly vulnerable to galvanic coupling. Therefore, microstructural manipulation does not play a key role in the corrosion behavior of the Zn alloys. Conversely, our results in Fig. 14 demonstrate the strong susceptibility of the CD Zn alloys to galvanic corrosion, resulting in severe localized pitting.

As extensively discussed in the previous section, the A4 CD wire experienced the dynamic precipitation of nanosized $AgZn_3$ particles, which were uniformly distributed throughout the

microstructure at the expense of Ag solutes in the Zn matrix (Figs. 6a and b). However, the $AgZn_3$ precipitates dissolve in the Zn grains after HT processing, increasing the concentration of Ag in the matrix. It is therefore hypothesized that the pitting corrosion is predominantly driven by the electrochemical potential difference between cathodic $AgZn_3$ and diluted Zn grains in the CD A4 wire. Indeed, the consumption of Ag from the Zn matrix during dynamic precipitation decreases the corrosion potential of Zn matrix and thereby boosts the galvanic coupling effect, which eventually causes an advanced level of pitting corrosion (Figs. 14a and b). Thus, it is concluded that the reduced galvanic corrosion sensitivity of the reported Zn alloys containing more noble elements (e.g. Cu and Ag) is because they all underwent hot processing (e.g. hot rolling and hot extrusion), which results in the formation of Zn solid solution grains along with relatively coarse second phases. Since the matrix in such alloys was enriched with the alloying element, the difference in corrosion potential between the matrix and second phases was small, decreasing the anodic activity of Zn matrix and eventually attenuating the galvanic corrosion. The CD A4 experienced an apparent localized pitting already after 10 days of immersion (Fig. 14a), while the surface of 20 s-HT A4 alloy (Fig. 14 c) was not affected by the corrosive attack and remained intact.

Similar to the binary alloy, localized corrosion of the multiphase CD AM46 wire with a noticeable quantity of $AgZn_3$ and Mn-rich particles is controlled by the microgalvanic coupling phenomenon (Figs. 14e and 14f). After HT, a substantial portion of Ag dissolves in Zn grains, whereas Mn-rich particles remain distributed at the grain boundaries (Fig. 12b). Consequently, HT reduces the volume fraction of $AgZn_3$ and the Zn matrix enriches with Ag. Thus, the microgalvanic effect between Zn solid solution matrix and anodic Mn particles/remaining $AgZn_3$ precipitates is not as strong due to the negligible difference in corrosion potentials between these phases (E_{corr} (vs SHE) = −1.19V, −076 V, and +0.8 V for Mn, Zn, and Ag, respectively). The beneficial effect of HT is more pronounced after longer immersion times. As shown in Figs. 14b and 14f, an initial localized attack on the CD wire (Figs. 14a and e) developed into clearly non-uniform morphology, showing the presence of deep pits on the entire sample surface. As noted earlier, such a feature is attributed to micro-galvanic activity between the diluted Zn solid solution matrix and $AgZn_3$/Mn-rich particles. Further, the higher volume of corrosion products observed for CD wires is due to the occurrence of non-homogenous dissolution promoted by localized attack (Fig. 14b and 14f). In contrast, interestingly, the localized corrosion in the HT wires is limited to smaller areas and the degradation advances in a relatively uniform corrosion mode even after 40 days of immersion (Figs 14h and 14d). In brief, the microstructural modification induced by HT significantly suppresses the localized corrosion attack in the HT A4 and AM46 wires.

Pitting corrosion initiates in areas where the protective layer is impaired by mechanical or chemical damage. In these areas the oxide/hydroxide/carbonate/phosphate film dissolves, leading to local destruction of the protective layer and the occurrence of localized corrosion (Figs. 14a, 14b and Figs. 14e, 14f). Additionally, dissolution or detachment of the surrounding film further exposes the Zn wire surface, which allows the pit to grow wider. Grain boundaries are possible locations for pit initiation and/or disruption of any protective film that covers the wire surface, due to the presence of $AgZn_3$. As a consequence, the protective film can be broken to expose the underlying alloy for further degradation. During

the immersion, Ag remains behind without dissolving and becomes concentrated on the alloy surface directly beneath the protective corrosion products (Figs. 14d, e, h - points D, E_2, H). It is not found in the surface protective film formed on the wires (Figs. 14a, f, points A_2, F_1).

As expected, due to the considerably high volume fraction of $AgZn_3$ precipitates and depletion of Ag from the Zn matrix, A4 and AM46 alloys in CD condition showed the highest degradation rates (Fig. 14m). Our results demonstrate that an adequate compromise between biodegradation rate and its uniformity could be achieved via microstructure design using an appropriate heat treatment strategy.

4. Conclusions

In this study, binary Zn-4.0Ag and ternary Zn-4.0Ag-*x*Mn (where *x*=0.2–0.6 wt%) alloys were investigated as possible candidates for bioresorbable stent applications. All materials were cast into ingots at 700 °C and solution-heat treated (at 400 °C for 2h-8h), followed by hot extrusion at 310 °C with an extrusion ratio of 39:1 to produce cylindrical rods with a diameter of 4 mm. Selected extruded alloys were wire drawn at room temperature without any interpass annealing. Cold drawn wires underwent a heat treatment process at 360°C for 2s to 60 min. The mechanical and corrosion properties of the alloys were investigated as a function of grain size and precipitates. Based on the results, the following conclusions are made:

- Hot extrusion of the binary Zn-4.0Ag alloy produced a fine equiaxed grain structure with the grain size of 18 μm, while Mn addition produced a bimodal grain structure, where the nucleated grains formed a necklace-type pattern around the coarse grains. Increasing the Mn content led to a further grain refinement due to the particle stimulated nucleation phenomenon.
- Increasing the Mn content monotonically improved the tensile strength from 267 MPa to 302 MPa for the Zn-4.0Ag-0.2Mn and the Zn-4.0Ag-0.6Mn alloys, respectively due to grain refinement and a higher volume fraction of Mn-rich particles. Alongside the improvement in tensile strength, the fracture elongation of the ternary alloys consistently increased from 25% to 35% for Zn-4.0Ag-0.2Mn and the Zn-4.0Ag-0.6Mn alloys, respectively. The elongation enhancement was attributed to the development of a random distribution of basal planes, which is more favorable for basal dislocation slip during tensile testing.
- Cold drawing resulted in the formation of an ultrafine-grained structure along with a dynamic precipitation of nanosized $AgZn_3$ particles in the binary and ternary alloys. Dynamic precipitation of the $AgZn_3$ phase is attributed to the considerably increased fraction of grain boundaries, acting as high-speed diffusion pathways.
- Alloys that underwent cold drawing (CD) exhibited a significant loss of tensile strength, strong strain rate sensitivity and pronounced strain softening. In addition, the CD binary alloy featured room temperature superplasticity (RTS), which was a result of the change in dominant flow mechanism from dislocation

slip to phase boundary sliding (PBS). In the case of the CD ternary alloy, the impeding effect of the Mn-rich particles on grain boundary mobility reduced the contribution of PBS and thereby suppressed the RTS.

- It was found that the tensile strength of the CD alloys with fine grains could not be explained by Hall-Petch relation when the grain sizes are smaller than critical alloy-specific values. The inverse Hall-Petch occurred at the grain sizes below 2.3 μm and 1.2 μm for Zn-4.0Ag and Zn-4.0Ag-0.6Mn, respectively.
- Short-time heat treatment could not only restore mechanical strength but also mitigated the strain softening and strain rate sensitivity of the alloys over a wide range of strain rates through a reduction in the number of deformation-induced $AgZn_3$ precipitates.
- The microstructural manipulation induced by CD markedly deteriorated the corrosion resistance of the Zn alloys in a manner that was associated with severe pitting. This is due to the fact that the dynamic precipitation was accompanied by the depletion of Ag from the Zn matrix, reducing the corrosion potential between diluted Zn matrix and precipitates. This promoted the microgalvanic effect between diluted Zn solid solution matrix and the anodic precipitates. However, the HT increased the corrosion potential of Zn matrix due to the dissolution of Ag into the Zn matrix and thereby reduced the localized corrosion.

The results and analysis of the present work provide fundamental insights into Zn-based alloys for stent applications. Specifically, an UFG structure should be avoided in Zn-based alloy stents. The UFG structure is accompanied by precipitation softening whereby the alloys experience mechanical degradation. Further, advanced processing techniques whereby non-equilibrium structures can be obtained (e.g. severe plastic deformation methods) are not recommended for Zn alloys since they boost the dynamic precipitation, which promotes mechanical instability. Finally, selection of Zn-based alloys for vascular stenting applications cannot rely on their mechanical and corrosion properties after thermomechanical processing of these materials because they differ drastically from those of the final stent products, which are subjected to cold drawing.

Acknowledgments

U.S. National Institute of Health - National Heart, Lung, and Blood Institute, Grant 1R01HL144739-01A1, and Michigan Tech College of Engineering, through Cross-Cutting Initiative funding, are acknowledged for funding this work. The authors would like to acknowledge the Engineering and Physical Sciences Research Council (EPSRC) grant EP/N032233/1 and the Henry Royce Institute for Advanced Materials, funded through EPSRC grants EP/R00661X/1 for JEOL JEM-F200 access at Royce@Sheffield. The authors also acknowledge the Applied Chemical and Morphological Analysis Laboratory (ACMAL) at Michigan Tech for using the instruments.

References:

[1]. Zheng YF, Gu XN, Witte F, Biodegradable metals, Materials Science and Engineering: R: Reports 77 (2014) 1–34.

[2]. Bowen PK, Shearier ER, Zhao S, Guillory RJ, Zhao F, Goldman J, Drelich JW, Biodegradable Metals for Cardiovascular Stents: from Clinical Concerns to Recent Zn-Alloys, Advanced Healthcare Materials 5(10) (2016) 1121–1140. [PubMed: 27094868]

[3]. Farb A, Weber DK, Kolodgie FD, Burke AP, Virmani R, Morphological predictors of restenosis after coronary stenting in humans, Circulation 105(25) (2002) 2974–2980. [PubMed: 12081990]

[4]. Pal N, Din J, O'Kane P, Contemporary Management of Stent Failure: Part One, Interv Cardiol 14(1) (2019) 10–16. [PubMed: 30858886]

[5]. Chung WS, Park CS, Seung KB, Kim PJ, Lee JM, Koo BK, Jang YS, Yang JY, Yoon JH, Kim DI, Yoon YW, Park JS, Cho YH, Park SJ, The incidence and clinical impact of stent strut fractures developed after drug-eluting stent implantation, Int. J. Cardiol 125(3) (2008) 325–331. [PubMed: 17434616]

[6]. Li H, Zheng Y, Qin L, Progress of biodegradable metals, Progress in Natural Science: Materials International 24(5) (2014) 414–422.

[7]. Witte F, Hort N, Vogt C, Cohen S, Kainer KU, Willumeit R, Feyerabend F, Degradable biomaterials based on magnesium corrosion, Current Opinion in Solid State and Materials Science 12(5–6) (2008) 63–72.

[8]. Mostaed E, Vedani M, Hashempour M, Bestetti M, Influence of ECAP process on mechanical and corrosion properties of pure Mg and ZK60 magnesium alloy for biodegradable stent applications, Biomatter 4 (2014) e28283. [PubMed: 25482411]

[9]. Pierson D, Edick J, Tauscher A, Pokorney E, Bowen P, Gelbaugh J, Stinson J, Getty H, Lee CH, Drelich J, Goldman J, A simplified in vivo approach for evaluating the bioabsorbable behavior of candidate stent materials, J. Biomed. Mater. Res. B Appl. Biomater 100(1) (2012) 58–67. [PubMed: 21905215]

[10]. Sikora-Jasinska M, Chevallier P, Turgeon S, Paternoster C, Mostaed E, Vedani M, Mantovani D, Understanding the effect of the reinforcement addition on corrosion behavior of Fe/Mg2Si composites for biodegradable implant applications, Mater. Chem. Phys 223 (2019) 771–778.

[11]. Bowen PK, Drelich J, Goldman J, Zinc Exhibits Ideal Physiological Corrosion Behavior for Bioabsorbable Stents, Advanced Materials 25(18) (2013) 2577–2582. [PubMed: 23495090]

[12]. Bowen PK, Guillory RJ 2nd, Shearier ER, Seitz JM, Drelich J, Bocks M, Zhao F, Goldman J, Metallic zinc exhibits optimal biocompatibility for bioabsorbable endovascular stents, Mater. Sci. Eng. C Mater. Biol. Appl 56 (2015) 467–72. [PubMed: 26249616]

[13]. Mostaed E, Sikora-Jasinska M, Drelich JW, Vedani M, Zinc-based alloys for degradable vascular stent applications, Acta Biomater. 71 (2018) 1–23. [PubMed: 29530821]

[14]. Mostaed E, Sikora-Jasinska M, Mostaed A, Loffredo S, Demir AG, Previtali B, Mantovani D, Beanland R, Vedani M, Novel Zn-based alloys for biodegradable stent applications: Design, development and in vitro degradation, J. Mech. Behav. Biomed. Mater 60 (2016) 581–602. [PubMed: 27062241]

[15]. Sikora-Jasinska M, Mostaed E, Mostaed A, Beanland R, Mantovani D, Vedani M, Fabrication, mechanical properties and in vitro degradation behavior of newly developed ZnAg alloys for degradable implant applications, Mater. Sci. Eng. C Mater. Biol. Appl 77 (2017) 1170–1181. [PubMed: 28531993]

[16]. Champagne S, Mostaed E, Safizadeh F, Ghali E, Vedani M, Hermawan H, In Vitro Degradation of Absorbable Zinc Alloys in Artificial Urine, Materials (Basel) 12(2) (2019).

[17]. Alves MM, Prošek T, Santos CF, Montemor MF, Evolution of the in vitro degradation of Zn-Mg alloys under simulated physiological conditions, RSC Advances 7(45) (2017) 28224–28233.

[18]. Li HF, Xie XH, Zheng YF, Cong Y, Zhou FY, Qiu KJ, Wang X, Chen SH, Huang L, Tian L, Qin L, Development of biodegradable Zn-1X binary alloys with nutrient alloying elements Mg, Ca and Sr, Sci. Rep 5 (2015) 10719. [PubMed: 26023878]

[19]. Shen C, Liu X, Fan B, Lan P, Zhou F, Li X, Wang H, Xiao X, Li L, Zhao S, Guo Z, Pu Z, Zheng Y, Mechanical properties, in vitro degradation behavior, hemocompatibility and cytotoxicity evaluation of Zn-1.2Mg alloy for biodegradable implants, RSC Advances 6(89) (2016) 86410–86419.

[20]. Niu J, Tang Z, Huang H, Pei J, Zhang H, Yuan G, Ding W, Research on a Zn-Cu alloy as a biodegradable material for potential vascular stents application, Mater. Sci. Eng. C Mater. Biol. Appl 69 (2016) 407–13. [PubMed: 27612729]

[21]. Tang Z, Huang H, Niu J, Zhang L, Zhang H, Pei J, Tan J, Yuan G, Design and characterizations of novel biodegradable Zn-Cu-Mg alloys for potential biodegradable implants, Materials & Design 117 (2017) 84–94.

[22]. Tang Z, Niu J, Huang H, Zhang H, Pei J, Ou J, Yuan G, Potential biodegradable Zn-Cu binary alloys developed for cardiovascular implant applications, J. Mech. Behav. Biomed. Mater 72 (2017) 182–191. [PubMed: 28499166]

[23]. Yue R, Huang H, Ke G, Zhang H, Pei J, Xue G, Yuan G, Microstructure, mechanical properties and in vitro degradation behavior of novel Zn-Cu-Fe alloys, Materials Characterization 134 (2017) 114–122.

[24]. Zhao S, McNamara CT, Bowen PK, Verhun N, Braykovich JP, Goldman J, Drelich JW, Structural Characteristics and In Vitro Biodegradation of a Novel Zn-Li Alloy Prepared by Induction Melting and Hot Rolling, Metallurgical and Materials Transactions A 48(3) (2017) 1204–1215.

[25]. Zhao S, Seitz JM, Eifler R, Maier HJ, Guillory RJ 2nd, Earley EJ, Drelich A, Goldman J, Drelich JW, Zn-Li alloy after extrusion and drawing: Structural, mechanical characterization, and biodegradation in abdominal aorta of rat, Mater. Sci. Eng. C Mater. Biol. Appl 76 (2017) 301–312. [PubMed: 28482531]

[26]. Li Z, Shi Z-Z, Hao Y, Li H-F, Liu X-F, Volinsky AA, Zhang H-J, Wang L-N, High-performance hot-warm rolled Zn-0.8Li alloy with nano-sized metastable precipitates and sub-micron grains for biodegradable stents, Journal of Materials Science & Technology (2019).

[27]. Dai Y, Zhang Y, Liu H, Fang H, Li D, Xu X, Yan Y, Chen L, Lu Y, Yu K, Mechanical strengthening mechanism of Zn-Li alloy and its mini tube as potential absorbable stent material, Materials Letters 235 (2019) 220–223.

[28]. Yin YX, Zhou C, Shi YP, Shi ZZ, Lu TH, Hao Y, Liu CH, Wang X, Zhang HJ, Wang LN, Hemocompatibility of biodegradable Zn-0.8wt% (Cu, Mn, Li) alloys, Mater. Sci. Eng. C Mater. Biol. Appl 104 (2019) 109896. [PubMed: 31499977]

[29]. Li P, Schille C, Schweizer E, Rupp F, Heiss A, Legner C, Klotz UE, Geis-Gerstorfer J, Scheideler L, Mechanical Characteristics, In Vitro Degradation, Cytotoxicity, and Antibacterial Evaluation of Zn-4.0Ag Alloy as a Biodegradable Material, Int. J. Mol. Sci 19(3) (2018).

[30]. Bowen PK, Seitz JM, Guillory RJ 2nd, Braykovich JP, Zhao S, Goldman J, Drelich JW, Evaluation of wrought Zn-Al alloys (1, 3, and 5 wt % Al) through mechanical and in vivo testing for stent applications, J. Biomed. Mater. Res. B Appl. Biomater 106(1) (2018) 245–258. [PubMed: 28130871]

[31]. Kafri A, Ovadia S, Goldman J, Drelich J, Aghion E, The Suitability of Zn-1.3%Fe Alloy as a Biodegradable Implant Material, Metals 8(3) (2018).

[32]. Wang Z, Zhang Q, Guo P, Gao X, Yang L, Song Z, Effects of laser surface remelting on microstructure and properties of biodegradable Zn-Zr alloy, Materials Letters 226 (2018) 52–54.

[33]. Zhu D, Cockerill I, Su Y, Zhang Z, Fu J, Lee KW, Ma J, Okpokwasili C, Tang L, Zheng Y, Qin YX, Wang Y, Mechanical Strength, Biodegradation, and in Vitro and in Vivo Biocompatibility of Zn Biomaterials, ACS Appl Mater Interfaces 11(7) (2019) 6809–6819. [PubMed: 30693753]

[34]. Werkhoven RJ, Sillekens WH, van Lieshout JBJM, Processing Aspects of Magnesium Alloy Stent Tube, in: Sillekens WH, Agnew SR, Neelameggham NR, Mathaudhu SN (Eds.), Magnesium Technology 2011, Springer International Publishing, Cham, 2016, pp. 419–424.

[35]. Zhang Y, Yan Y, Xu X, Lu Y, Chen L, Li D, Dai Y, Kang Y, Yu K, Investigation on the microstructure, mechanical properties, in vitro degradation behavior and biocompatibility of newly developed Zn-0.8%Li-(Mg, Ag) alloys for guided bone regeneration, Mater. Sci. Eng. C Mater. Biol. Appl 99 (2019) 1021–1034. [PubMed: 30889634]

[36]. Guillory RJ 2nd, Sikora-Jasinska M, Drelich JW, Goldman J, In Vitro Corrosion and in Vivo Response to Zinc Implants with Electropolished and Anodized Surfaces, ACS Appl Mater Interfaces 11(22) (2019) 19884–19893. [PubMed: 31058494]

[37]. Callister WD, Rethwisch DG, Materials Science and Engineering: An Introduction, Wiley (2010).

[38]. Mostaed E, Ardakani MS, Sikora-Jasinska M, Drelich JW, Precipitation induced room temperature superplasticity in Zn-Cu alloys, Materials Letters 244 (2019) 203–206. [PubMed: 31871366]

[39]. Wagoner RH, Strain-rate sensitivity of zinc sheet, Metallurgical and Materials Transactions A 15(6) (1984) 1265–1271.

[40]. Stoeckel D, Bonsignore C, Duda S, A survey of stent designs, Minim. Invasive Ther. Allied Technol 11(4) (2002) 137–147. [PubMed: 16754063]

[41]. Hersent E, Marthinsen K, Nes E, On the Effect of Atoms in Solid Solution on Grain Growth Kinetics, Metallurgical and Materials Transactions A 45(11) (2014) 4882–4890.

[42]. Mostaed E, Hashempour M, Fabrizi A, Dellasega D, Bestetti M, Bonollo F, Vedani M, Microstructure, texture evolution, mechanical properties and corrosion behavior of ECAP processed ZK60 magnesium alloy for biodegradable applications, J. Mech. Behav. Biomed. Mater 37 (2014) 307–22. [PubMed: 24971801]

[43]. Robson JD, Henry DT, Davis B, Particle effects on recrystallization in magnesium-manganese alloys: Particle-stimulated nucleation, Acta Materialia 57(9) (2009) 2739–2747.

[44]. Fiebig J, Divinski S, Rösner H, Estrin Y, Wilde G, Diffusion of Ag and Co in ultrafine-grained α-Ti deformed by equal channel angular pressing, Journal of Applied Physics 110(8) (2011).

[45]. Shi Z-Z, Li Z-L, Bai W-S, Tuoliken A, Yu J, Liu X-F, (Fe, Mn)Zn13 phase and its core-shell structure in novel biodegradable Zn-Mn-Fe alloys, Materials & Design 162 (2019) 235–245.

[46]. Shi Z-Z, Li H-Y, Xu J-Y, Gao X-X, Liu X-F, Microstructure evolution of a high-strength low-alloy Zn-Mn-Ca alloy through casting, hot extrusion and warm caliber rolling, Materials Science and Engineering: A (2019) 138626.

[47]. Nicola Ecob B Ralph, The effect of grain size on deformation twinning in a textured zinc alloy, Journal of Materials Science 18 (1983) 2419–2429.

[48]. Trelewicz JR, Schuh CA, The Hall-Petch breakdown in nanocrystalline metals: A crossover to glass-like deformation, Acta Materialia 55(17) (2007) 5948–5958.

[49]. Wang L, He Y, Zhao H, Xie H, Li S, Ren Y, Qin G, Effect of cumulative strain on the microstructural and mechanical properties of Zn-0.02 wt%Mg alloy wires during room-temperature drawing process, Journal of Alloys and Compounds 740 (2018) 949–957.

[50]. Wątroba M, Bednarczyk W, Kawałko J, Mech K, Marciszko M, Boelter G, Banzhaf M, Bała P, Design of novel Zn-Ag-Zr alloy with enhanced strength as a potential biodegradable implant material, Materials & Design 183 (2019).

[51]. Qiang G, Mostaed E, Zanella C, Zhentao Y, Vedani M, Ultra-Fine Grained Degradable Magnesium for Biomedical Applications, Rare Metal Materials and Engineering 43(11) (2014) 2561–2566.

[52]. Nie FL, Zheng YF, Wei SC, Hu C, Yang G, In vitro corrosion, cytotoxicity and hemocompatibility of bulk nanocrystalline pure iron, Biomed. Mater 5(6) (2010) 065015. [PubMed: 21079282]

[53]. Christian JW, Mahajan S, Deformation twinning, Progress in Materials Science 39(1) (1995) 1–157.

[54]. Langdon TG, Seventy-five years of superplasticity: historic developments and new opportunities, Journal of Materials Science 44(22) (2009) 5998–6010.

[55]. Mostaed E, Fabrizi A, Dellasega D, Bonollo F, Vedani M, Grain size and texture dependence on mechanical properties, asymmetric behavior and low temperature superplasticity of ZK60 Mg alloy, Materials Characterization 107 (2015) 70–78.

[56]. Mostaed E, Fabrizi A, Dellasega D, Bonollo F, Vedani M, Microstructure, mechanical behavior and low temperature superplasticity of ECAP processed ZM21 Mg alloy, Journal of Alloys and Compounds 638 (2015) 267–276.

[57]. Langdon TG, Twenty-five years of ultrafine-grained materials: Achieving exceptional properties through grain refinement, Acta Materialia 61(19) (2013) 7035–7059.

[58]. Watanabe H, Mukai T, Higashi K, Influence of Temperature and Grain Size on Threshold Stress for Superplastic Flow in a Fine-Grained Magnesium Alloy, Metallurgical and Materials Transactions A 39(10) (2008) 2351–2362.

[59]. Bednarczyk W, Kawałko J, Wątroba M, Bała P, Achieving room temperature superplasticity in the Zn-0.5Cu alloy processed via equal channel angular pressing, Materials Science and Engineering: A 723 (2018) 126–133.

[60]. Bednarczyk W, Wątroba M, Kawałko J, Bała P, Can zinc alloys be strengthened by grain refinement? A critical evaluation of the processing of low-alloyed binary zinc alloys using ECAP, Materials Science and Engineering: A 748 (2019) 357–366.

[61]. Song D, Ma A, Jiang J, Lin P, Yang D, Fan J, Corrosion behavior of equal-channel-angular-pressed pure magnesium in NaCl aqueous solution, Corrosion Science 52(2) (2010) 481–490.

Statement of significance

Owing to its promising biodegradability, zinc has been recognized as a potential biodegradable material for stenting applications. However, Zn's poor strength alongside intrinsic mechanical instability have propelled researchers to search for Zn alloys with improved mechanical properties. Although extensive researches have been conducted to satisfy the mentioned concerns, no Zn-based alloys with stabilized mechanical properties have yet been reported. In this work, the mechanical properties and stability of the Zn-Ag-based alloys were systematically evaluated as a function of microstructural features. We found that the microstructure design in Zn alloys can be used to find an effective strategy to not only improve the strength and suppress the mechanical instability but also to minimize any damage by augmenting the corrosion uniformity.

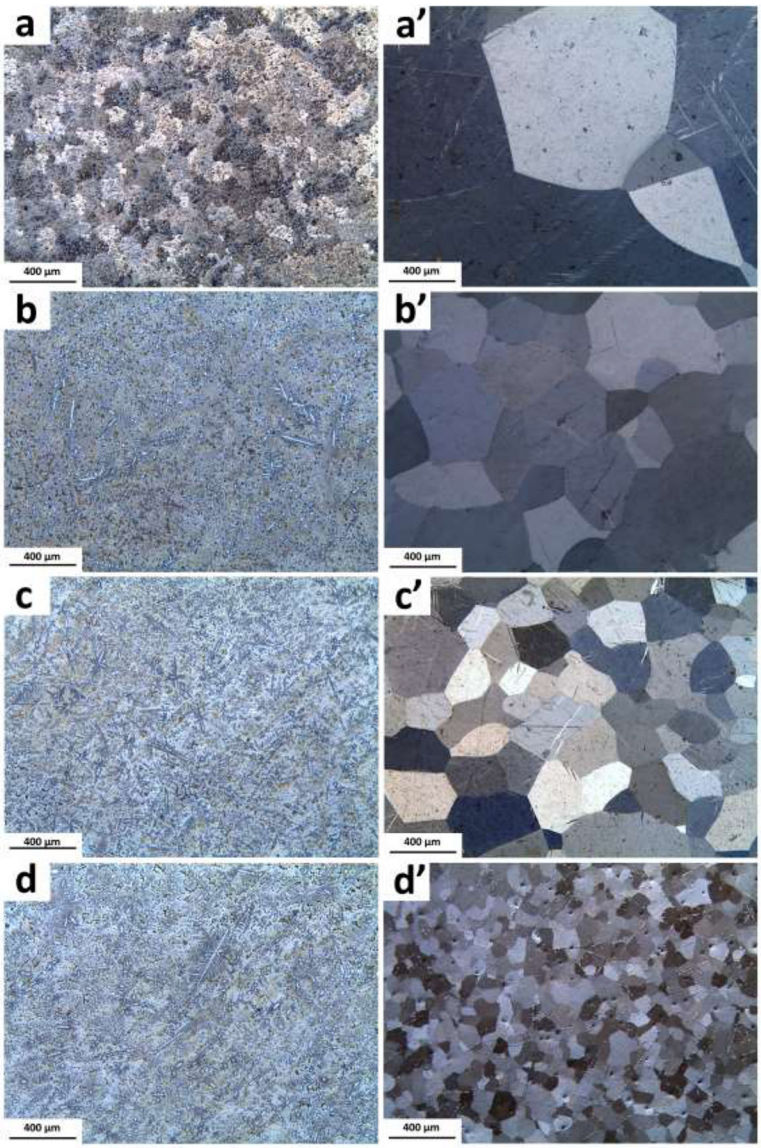

Fig. 1.

Optical microstructure of the as-cast alloys: (a) A4, (b) AM42, c) AM44, (d) AM46 and their corresponding solution heat-treated (a'–d').

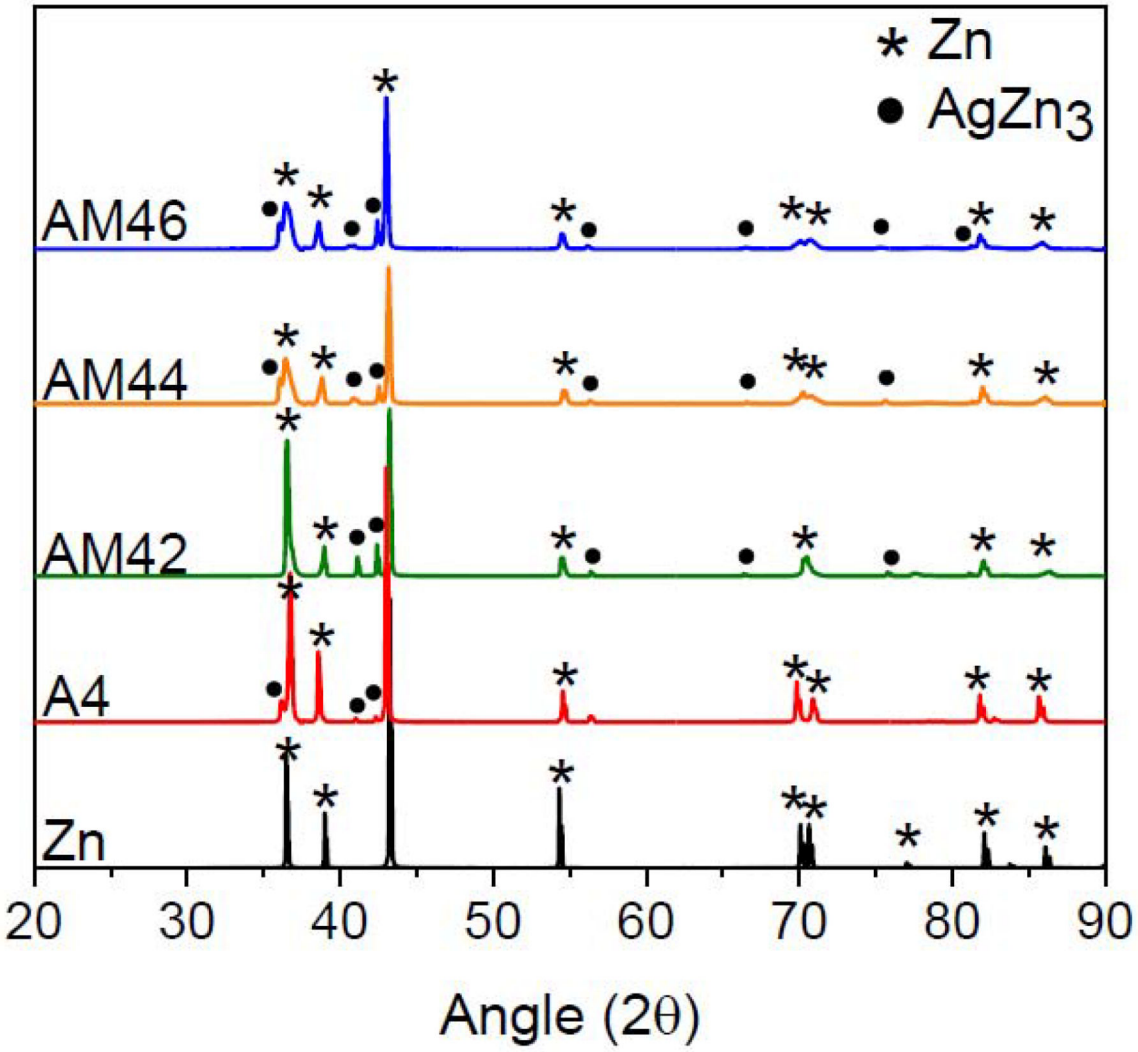

Fig. 2.
XRD patterns of the investigated alloys in the as-cast condition.

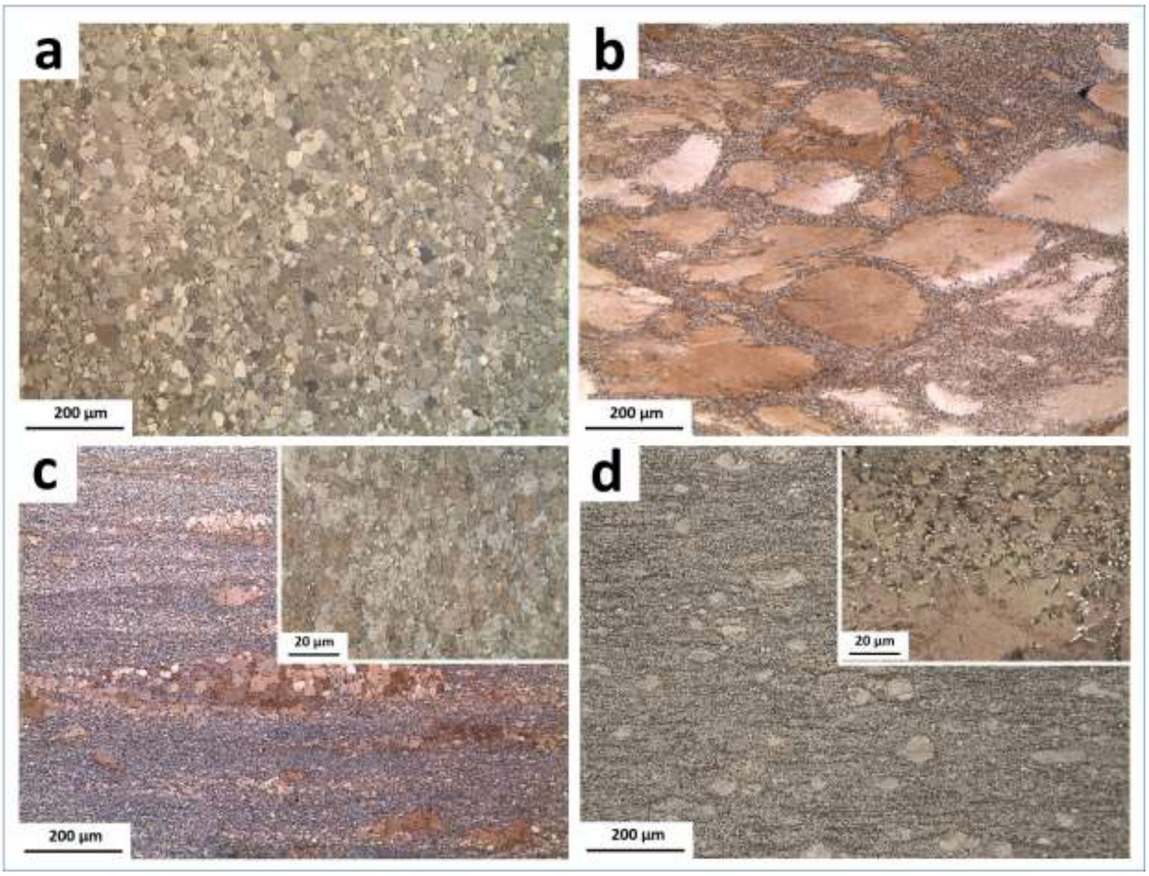

Fig. 3.
Microstructure of the extruded alloys: (a) A4, (b) AM42, (c) AM44 and (d) AM46.

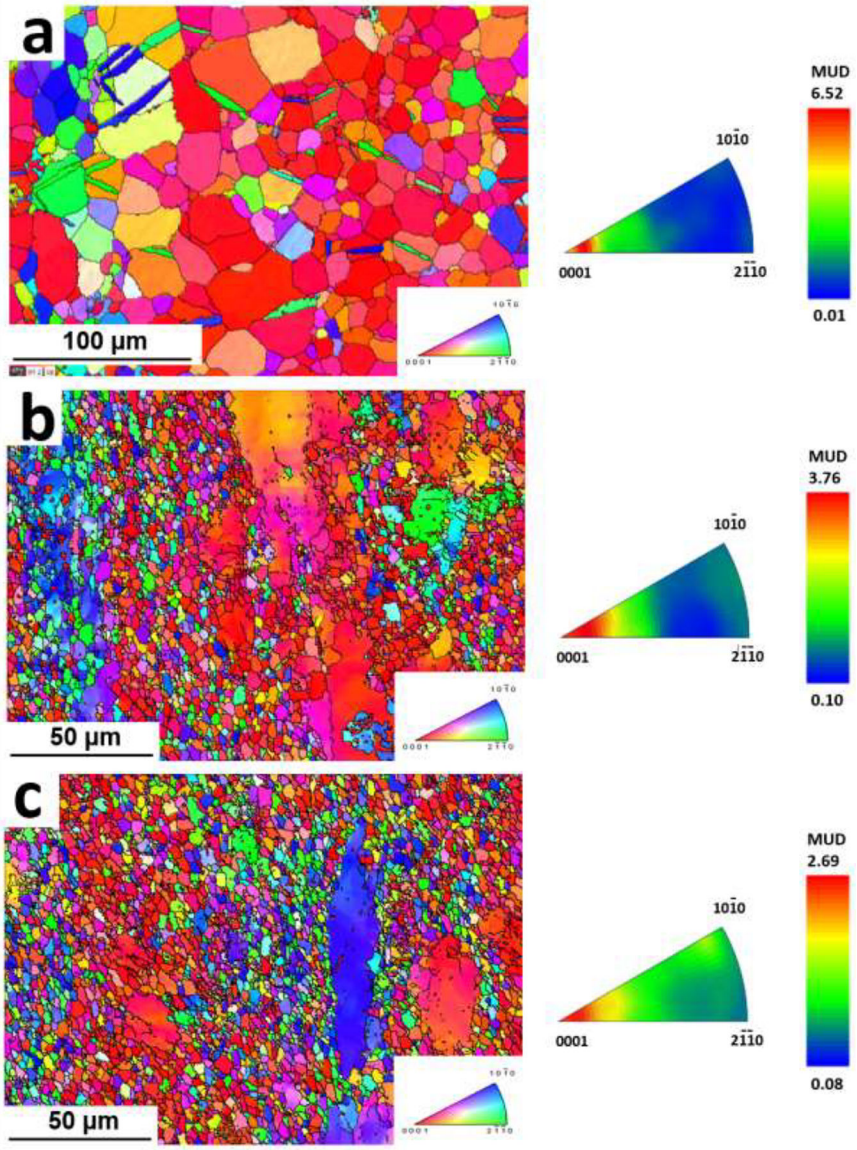

Fig. 4.
IPF map of the extruded (a) A4, (b) AM44 and (c) AM46 alloys.

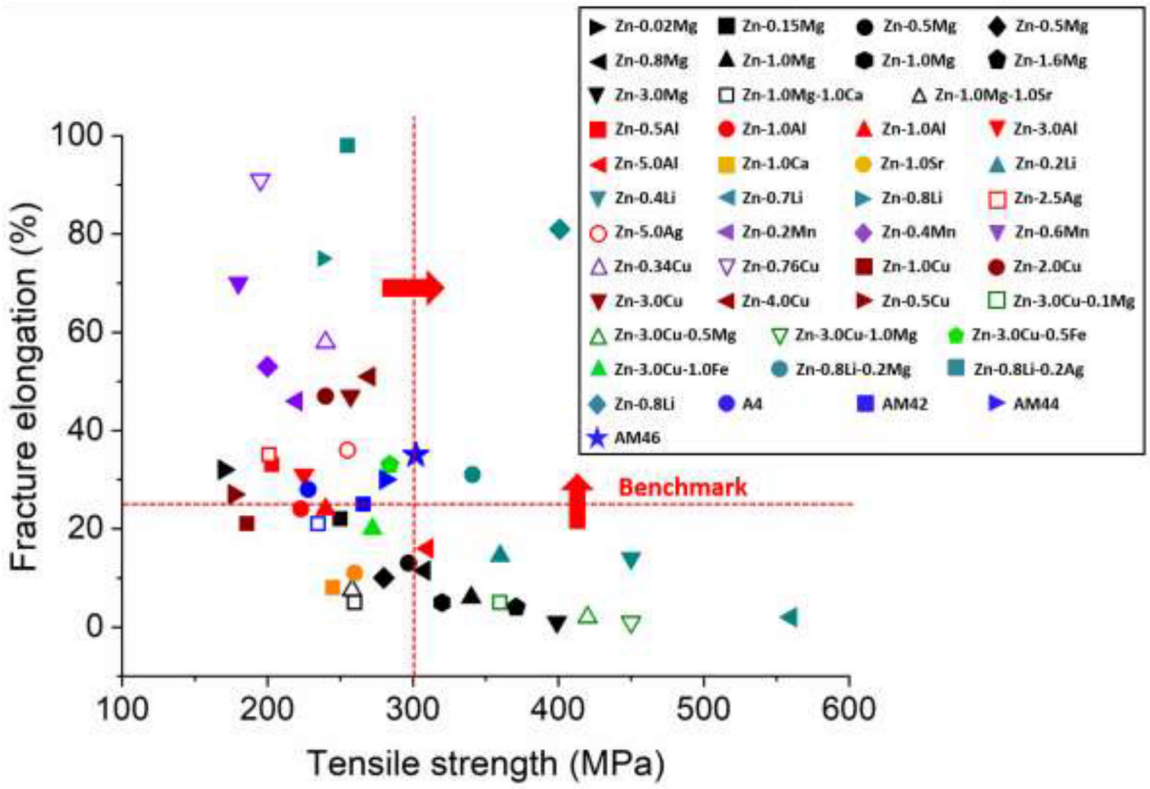

Fig. 5.

Mechanical properties of the investigated Zn-Ag-based alloys compared to Zn alloys explored so far [13, 14, 26, 35].

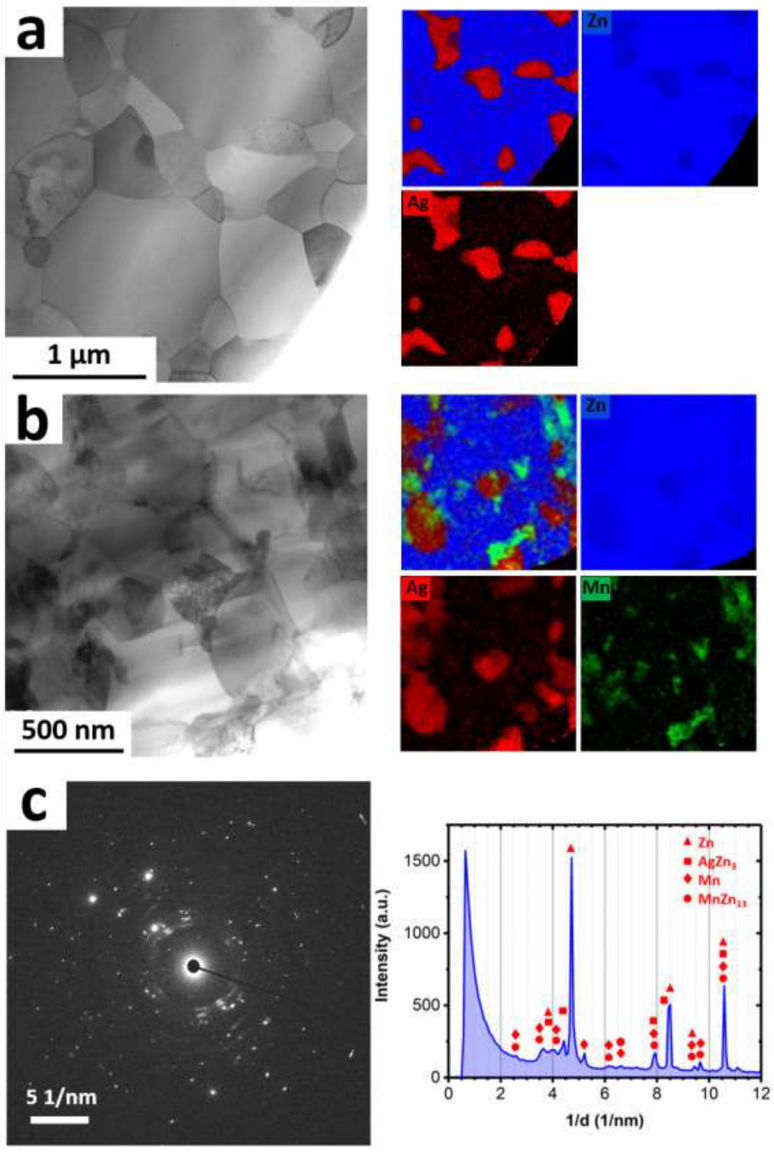

Fig. 6.

Bright field STEM images and their corresponding EDS elemental maps obtain from the CD (a) A4 and (b) AM46 alloys. (c) SAD pattern obtained from the AM46 alloy showing reflections for the Zn, $AgZn_3$ and Mn phases.

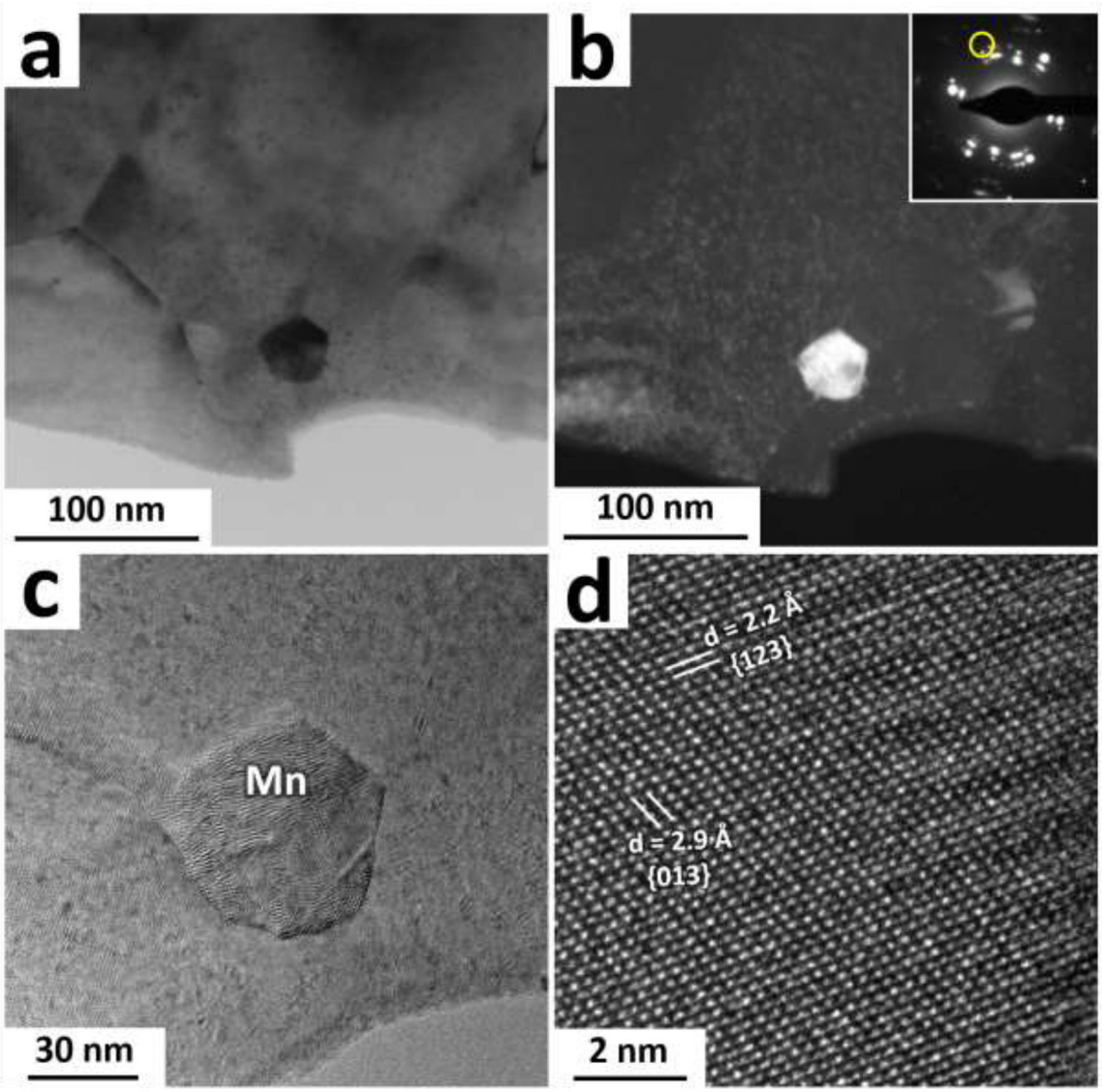

Fig. 7.

(a) Bright field TEM image obtained from the AM46 alloy. (b) Dark field TEM image from the area shown in (a) which is formed by screening those diffracted beam marked by a yellow circle (i.e. 1/d ≈ 5.3 1/nm and 1/d ≈ 5.5 1/nm) in the inset. (c) and (d) display high resolution TEM images obtained from the Mn particle shown in (a) at different magnifications.

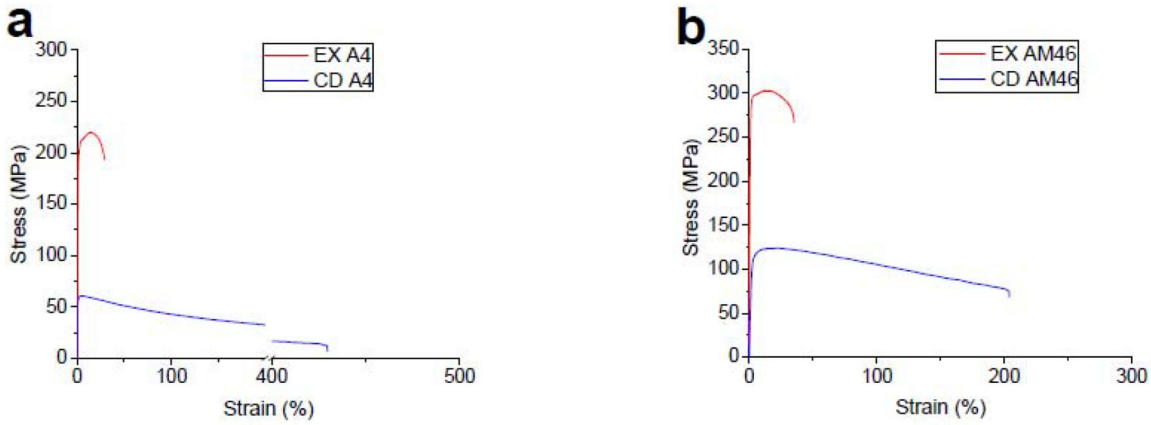

Fig. 8.

Engineering stress-strain tensile curves for (a) A4 and (b) AM46 alloys in EX and CD conditions.

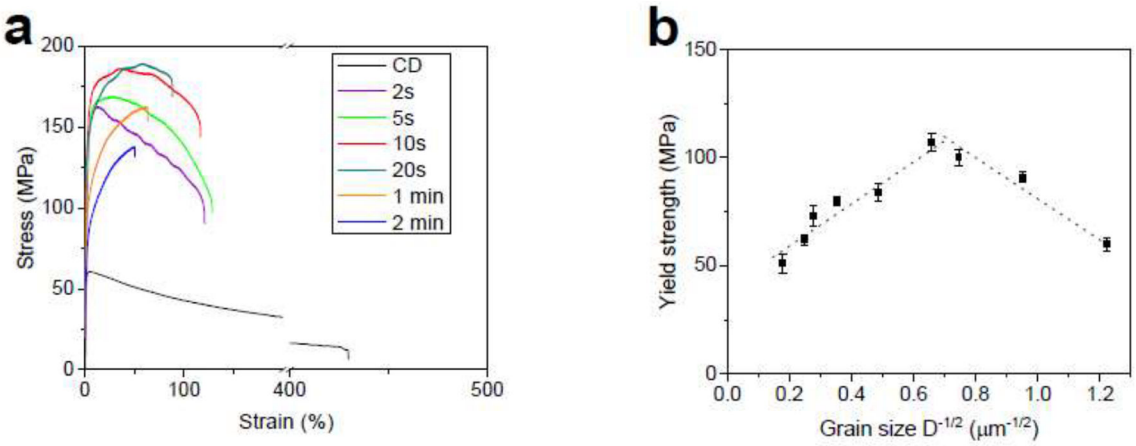

Fig. 9.

(a) tensile curves for the CD A4 alloy at different HT times and (b) their corresponding Hall-Petch relationship.

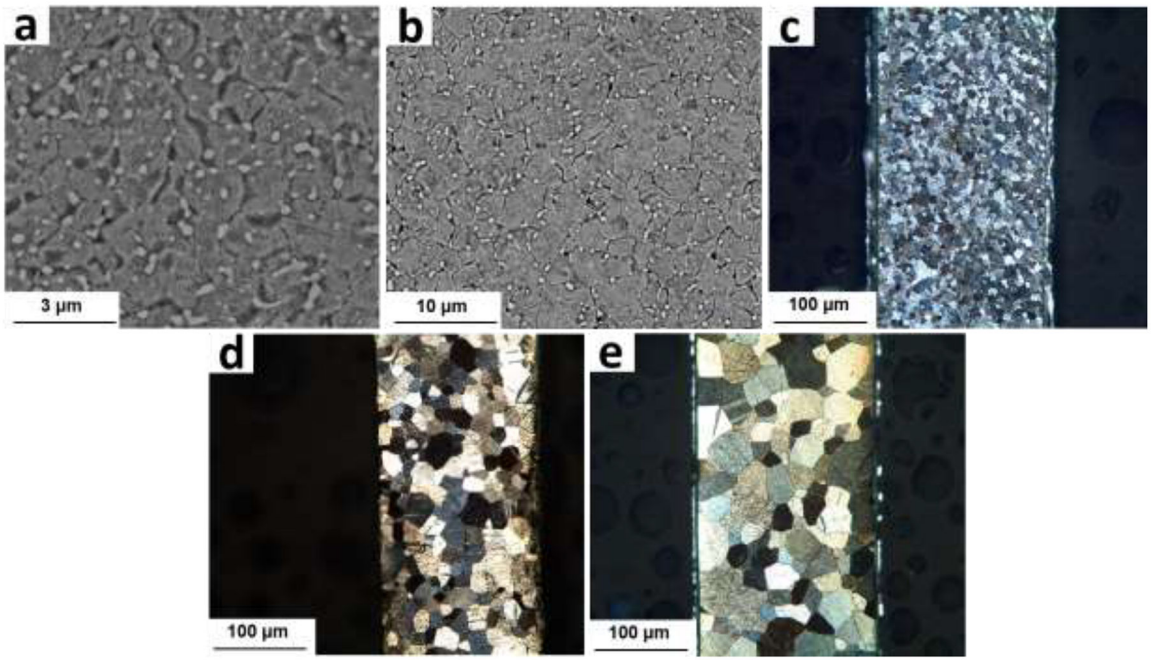

Fig. 10.
Microstructure of the CD A4 alloy after (a) 2s (b) 10s, (c) 20s, (d) 1 min and (e) 2 min of HT.

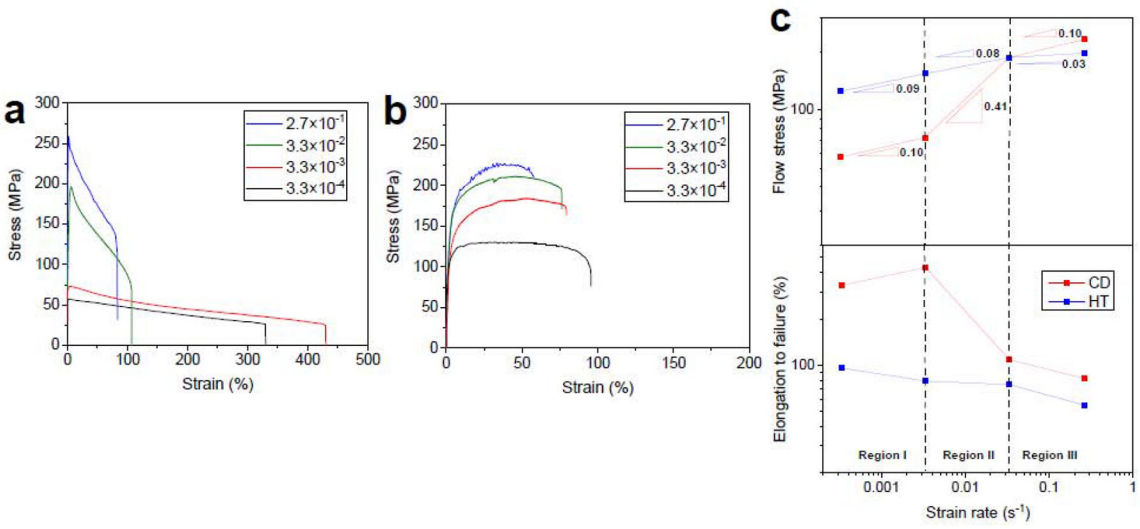

Fig. 11.

The effect of strain rate on the engineering stress-strain curves for the (a) CD and (b) 20 s-annealed A4 alloy. (c) the variation of flow stress and fracture elongation versus strain rates obtained from (a) and (b).

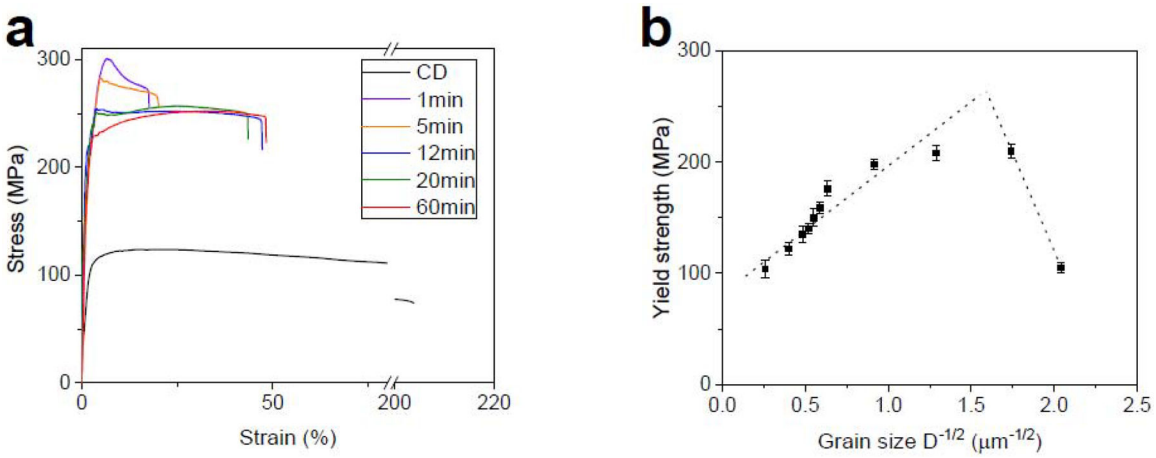

Fig. 12.

(a) tensile curves of the CD AM46 alloy at different HT times and (b) their corresponding Hall-Petch relationship.

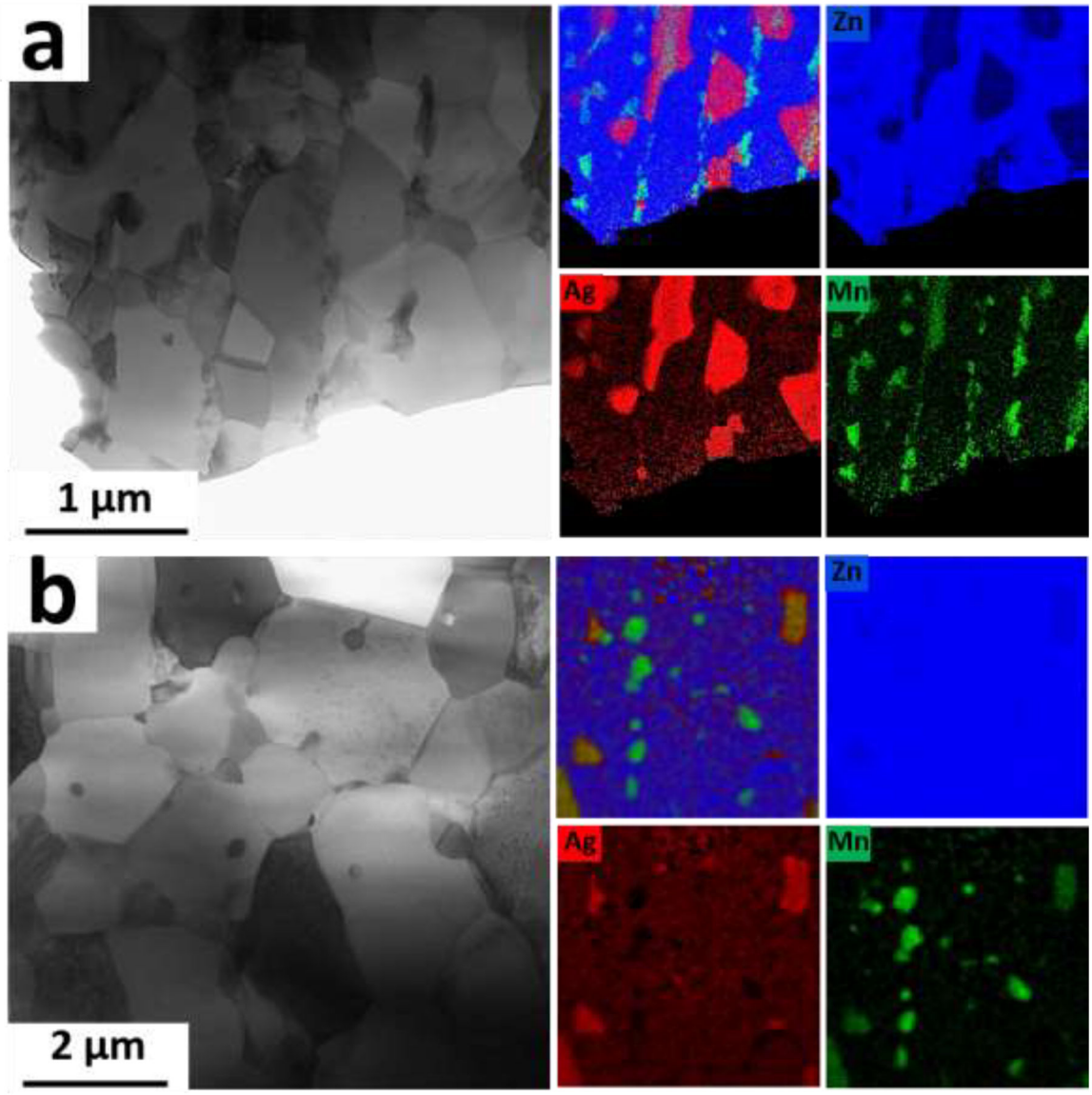

Fig. 13.

Bright field STEM images obtained from the AM46 alloy after (a) 1 min and (b) 20 min of HT and their corresponding EDS elemental maps.

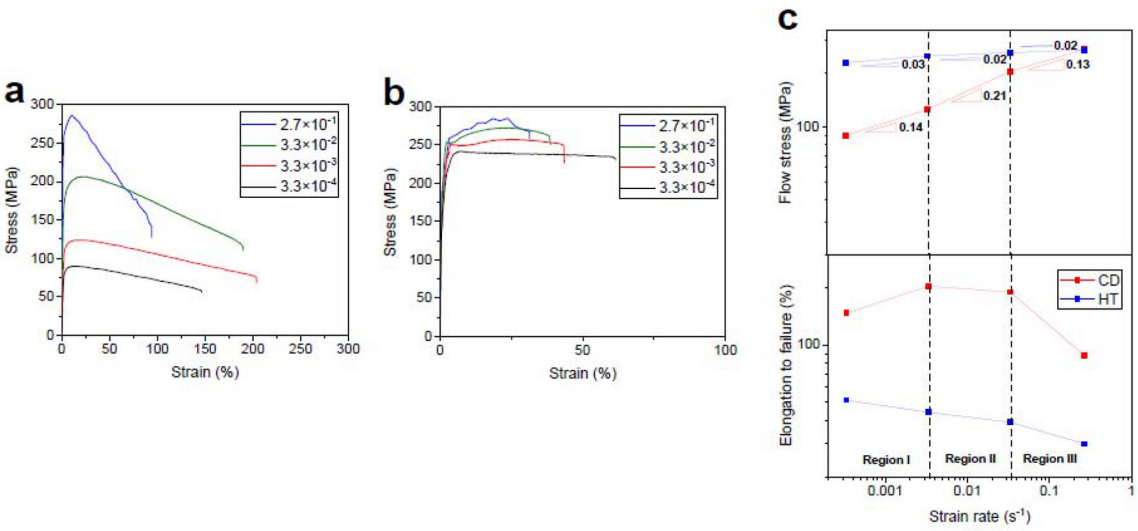

Fig. 14.

The effect of strain rate on the engineering stress-strain curves for the (a) CD and (b) 20 min-HT AM46 alloy. (c) the variation of flow stress versus strain rates obtained from (a) and (b).

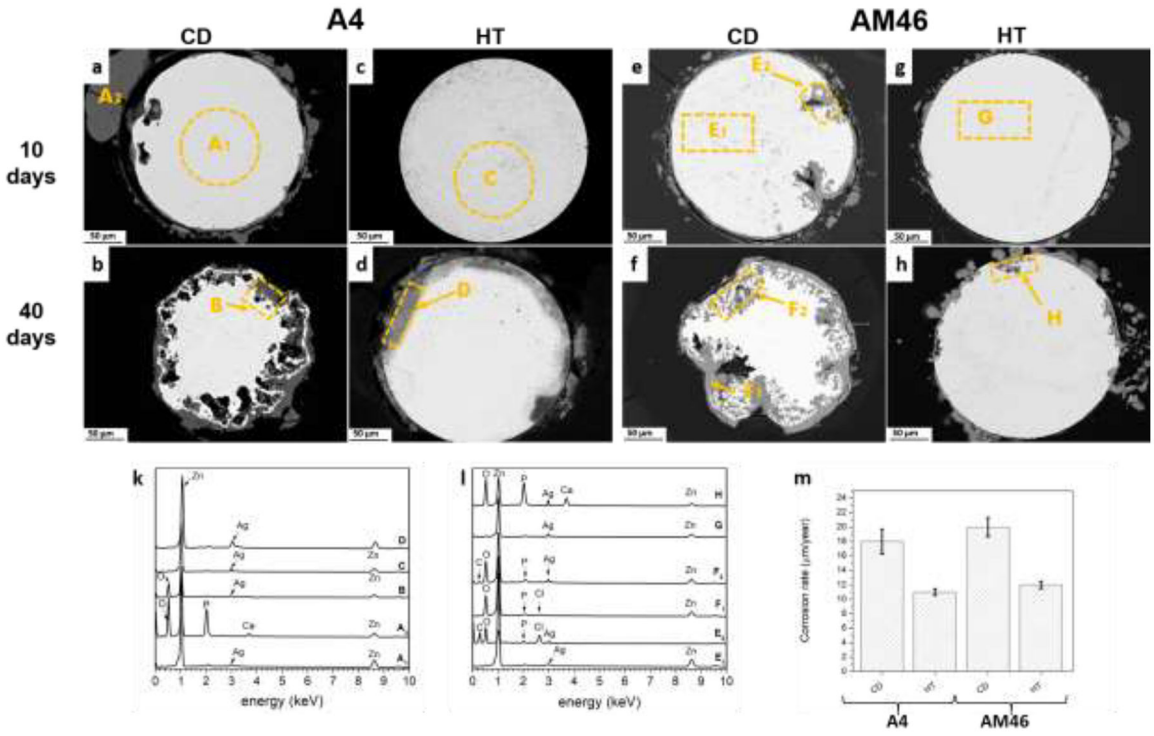

Fig. 15.

Cross-sectional morphologies of the corroded A4 (a-d) and AM46 wires (e-h) after 10 (a, c, e, g) and 40 days (b, d, f, h) of static immersion tests, (k, l) corresponding EDS analyses, and (m) corrosion rates on the wires after 40 days of immersion tests.

Table 1.

Composition of the investigated alloys.

	Alloy		Ag (wt.%)	Mn (wt.%)	Zn (wt.%)
1	**A4**	Zn-4.0Ag	4.0	-	Balance
2	**AM42**	Zn-4.0Ag-0.2Mn	4.0	0.2	Balance
3	**AM44**	Zn-4.0Ag-0.4Mn	4.0	0.4	Balance
4	**AM46**	Zn-4.0Ag-0.6Mn	4.0	0.6	Balance